Selective catalysis remedies polysulfide shuttling in lithium-sulfur batteries

Wuxing Hua
School of Chemical Engineering and Technology, Tianjin University, Tianjin 300072, China
Huan Li
School of Chemical Engineering and Advanced Materials, The University of Adelaide, Adelaide, SA 5005, Australia;
Chun Pei
Key Laboratory of Resource Chemistry of Ministry of Education, Shanghai Key Laboratory of Rare Earth Functional Materials, Department of Chemistry, Shanghai Normal University, Shanghai 200234, China
Jingyi Xia
School of Chemical Engineering and Technology, Tianjin University, Tianjin 300072, China
Yafei Sun
Shanghai Normal University
Chen Zhang
Tianjin University
Wei Lv
Tsinghua University
Ying Tao
Nanoyang Group, State Key Laboratory of Chemical Engineering, School of Chemical Engineering and Technology, Tianjin University, Tianjin 300072, China
Yan Jiao
The University of Adelaide https://orcid.org/0000-0003-1329-4290
Bingsen Zhang
Institute of Metal Research, Chinese Academy of Sciences https://orcid.org/0000-0002-2607-2999
Shizhang Qiao
University of Adelaide https://orcid.org/0000-0002-4568-8422
Ying Wan
Shanghai Normal University https://orcid.org/0000-0002-6898-6748
Quan-Hong Yang (qhyangcn@tju.edu.cn)
School of Chemical Engineering and Technology, Tianjin University, Tianjin 300072, China

Article

Keywords: polysulfide shuttling, lithium-sulfur batteries, catalysis

Posted Date: December 1st, 2020

DOI: https://doi.org/10.21203/rs.3.rs-98178/v1

Version of Record: A version of this preprint was published at Advanced Materials on August 2nd, 2021.
See the published version at https://doi.org/10.1002/adma.202101006.

Selective catalysis remedies polysulfide shuttling in lithium-sulfur batteries

Wuxing Hua[1,2†], Huan Li[3†], Chun Pei[2†], Jingyi Xia[1], Yafei Sun[2], Chen Zhang[4], Wei Lv[5], Ying Tao[1], Yan Jiao[3], Bingsen Zhang[6], Shi-Zhang Qiao[3], Ying Wan[2]* and Quan-Hong Yang[1]*

The shuttling of soluble lithium polysulfides between the electrodes leads to serious capacity fading and excess use of electrolyte, which severely bottlenecks practical use of Li-S batteries. Here selective catalysis is proposed as a fundamental remedy for the consecutive solid-liquid-solid sulfur redox reactions. The proof-of-concept In_2O_3 catalyst targetedly slows down the solid-liquid conversion, dissolution of elemental sulfur to polysulfides, while accelerates the liquid-solid conversion, deposition of polysulfides into insoluble Li_2S, which basically reduces accumulation of polysulfides in electrolyte, finally inhibiting the shuttle effect. The selective catalysis is revealed, experimentally and theoretically, by changes of activation energies and kinetic currents, modified reaction pathway together with the probed $LiInS_2$ intermediates, and gradual deactivation of the catalyst. The In_2O_3-catalysed Li-S battery works steadily over 1000 cycles at 4.0 C and yields an initial areal capacity up to 9.4 mAh cm^{-2} with a sulfur loading of ~9.0 mg cm^{-2}.

[1]Nanoyang Group, State Key Laboratory of Chemical Engineering, School of Chemical Engineering and Technology, Tianjin University, Tianjin 300350, China; [2]Key Laboratory of Resource Chemistry of Ministry of Education, Shanghai Key Laboratory of Rare Earth Functional Materials, Department of Chemistry, Shanghai Normal University, Shanghai 200234, China; [3]School of Chemical Engineering and Advanced Materials, The University of Adelaide, Adelaide, SA 5005, Australia; [4]School of Marine Science and Technology, Tianjin University, Tianjin 300072, China; [5]Shenzhen Key Laboratory for Graphene-based Materials and Engineering Laboratory for Functionalized Carbon Materials, Graduate School at Shenzhen, Tsinghua University, Shenzhen 518055, China; [6]Shenyang National Laboratory for Materials Science, Institute of Metal Research, Chinese Academy of Sciences, Shenyang 110016, China. [†]These authors are equal main contributors. Corresponding E-mails: ywan@shnu.edu.cn; qhyangcn@tju.edu.cn.

Introduction

Lithium-sulfur (Li-S) batteries show great promise among future battery techniques due to their theoretically high energy density (~2600 Wh kg^{-1}), low cost and environmental benign.[1-2] However, their real use in large scale is still plagued with challenges, such as the poor electrical conductivity of sulfur and solid-state discharge products (Li_2S/Li_2S_2), and the large volume change (~80%) of the sulfur cathode during cycling.[3-4] The operation of Li-S batteries involves solid-liquid-solid consecutive reactions both for the discharge and charge process and creates a series of polysulfide ions (LiPSs, also denoted Li_2S_n, $4 \leqslant n \leqslant 8$) that are soluble and mobile in the organic electrolytes. Thus, a more serious problem for the practical Li-S batteries is the shuttling of the soluble Li_2S_n from the cathode to anode side to form non-reusable solid Li_2S_2/Li_2S, which causes the so-called "shuttle effect". This bottlenecks the real applications with rapid capacity fade (short cycling life) and excess use of electrolyte (far lower energy density than the theoretical value).[3, 5-6] Physical confinement (Schemes 1a) mostly with porous carbons and chemical anchoring (Schemes 1b) by polar substrates are commonly used to inhibit the shuttle effect.[7-13] However, both strategies intrinsically are passive solutions, where Li_2S_n are "confined" and "blocked" in the cathode system. The shuttle effect is basically driven by the concentration gradient of the soluble Li_2S_n,[3] and thus a root solution is required that accelerates the conversion of Li_2S_n in the sulfur reduction reaction (SRR, corresponding to discharge process) and sulfur evolution reaction (SER, corresponding to charge process) to reduce the opportunities of the Li_2S_n shuttling and finally suppressing the shuttle effect.

Catalysis has recently been introduced into Li-S batteries as such a proactive strategy for accelerating the conversion of Li_2S_n and thereby tackling the shuttle effect,[14, 15] and sulfides, nitrides, phosphides and their heterostructures were employed as the catalysts.[16-25] Most recently, Peng et al. have presented a fundamental look at the catalysis in Li-S batteries.[26] Specially, they directly profile the electron-transfer numbers to characterize the electrocatalytic sulfur reduction and confirm catalysis as a promising pathway to tackle the fundamental challenges for Li-S batteries. However, what is the "right" catalyst for Li-S batteries towards a practical application remains unclear. The root cause of the shuttle effect is the accumulation of soluble Li_2S_n in the consecutive solid-liquid-solid reactions, and therefore, as shown in Scheme 1c, we propose that an ideal catalyst for the discharge process is expected not only to accelerates the liquid-solid reaction, deposition of Li_2S_n into insoluble Li_2S, as reported widely,[15] but also to slow down the previous step of solid-liquid reaction, dissolution of elemental sulfur to Li_2S_n; the composition of "accelerating" and "slowing-down" basically reduces the accumulation of polysulfides in the

electrolyte, providing a fundamental scheme for inhibiting the shuttle effect.

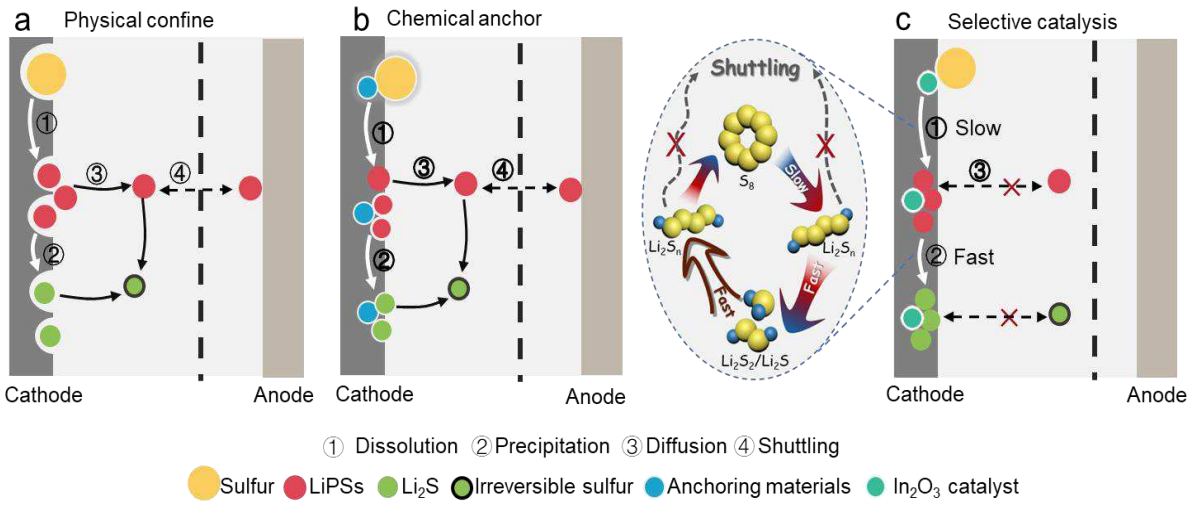

Scheme 1 Strategies to tackcle "shuttle effect" of soluble lithium polysulfides (Li_2S_n): physical confinement (a), chemical anchoring (b) and selective catalysis (c). Physical confinement and chemical anchoring are the most common ways to trap the soluble Li_2S_n, working as follows: 1) the elemental sulfur gets electrons and forms Li_2S_n on the conductive substrate; 2) the trapped Li_2S_n are further reduced to Li_2S on the conductive substrate; 3) other Li_2S_n are released from the conductive substrate and dissolved in the electrolyte; 4) Some of the dissolved Li_2S_n shuttle to the lithium metal side and then transfer back to the cathode side, resulting in the shuttle effect; the shuttled Li_2S_n result in a continuous loss of active sulfur and the corrosion of Li anodes. Selective catalysis is proposed in this study as a fundamental remedy for reducing the accummulation of soluble Li_2S_n and finally inhibiting the shuttle effect. For the discharging, the catalysis selectively slows down dissolution of elemental sulfur to Li_2S_n while accelerates the deposition of Li_2S_n into insoluble Li_2S.

In this work, we use nanoparticulated indium oxides (In_2O_3 NP) as a proof-of-concept catalyst to demonstrate the selective catalysis for the consecutive solid-liquid-solid reaction, which is not only confirmed by the changes of kinetic currents and activation energies of different steps of sulfur redox reaction, but also in-situ monitoring of the modified reaction pathway together with the probed catalytic intermediate, $LiInS_2$, as well as the featured catalyst deactivation. The SRR process (discharge) of the assembled battery well characterizes the selective catalysis, where the In_2O_3 catalyst, with strong adsorption towards elemental sulfur, slows down the dissolution of elemental sulfur to soluble Li_2S_n, while accelerates the Li_2S_n disposition to insoluble Li_2S due to the strong catalytic ability with $LiInS_2$ intermediates. For the SER process (charge), the catalysis with the probed $LiInS_2$ intermediates greatly reduces the energy barrier of Li_2S being oxidized to Li_2S_n and eventually converted to elemental sulfur, which, however, is hardly accomplished in the catalyst-free cell under the same charge voltage. Benefiting from the catalysis, the Li-S battery cell shows a good cycling stability and works steadily with negligible capacity decay over 1000 cycles at an ultrahigh

rate of 4.0 C; moreover, the battery displays a high initial areal capacity up to 9.4 mAh cm^{-2} at a current density of 0.9 mA cm^{-2} even with a high sulfur loading (~9.0 mg cm^{-2}). This work featured with selective catalysis rightly indicates a rational design principle for the catalysts towards a practical Li-S battery with suppressed shuttle effect.

Results

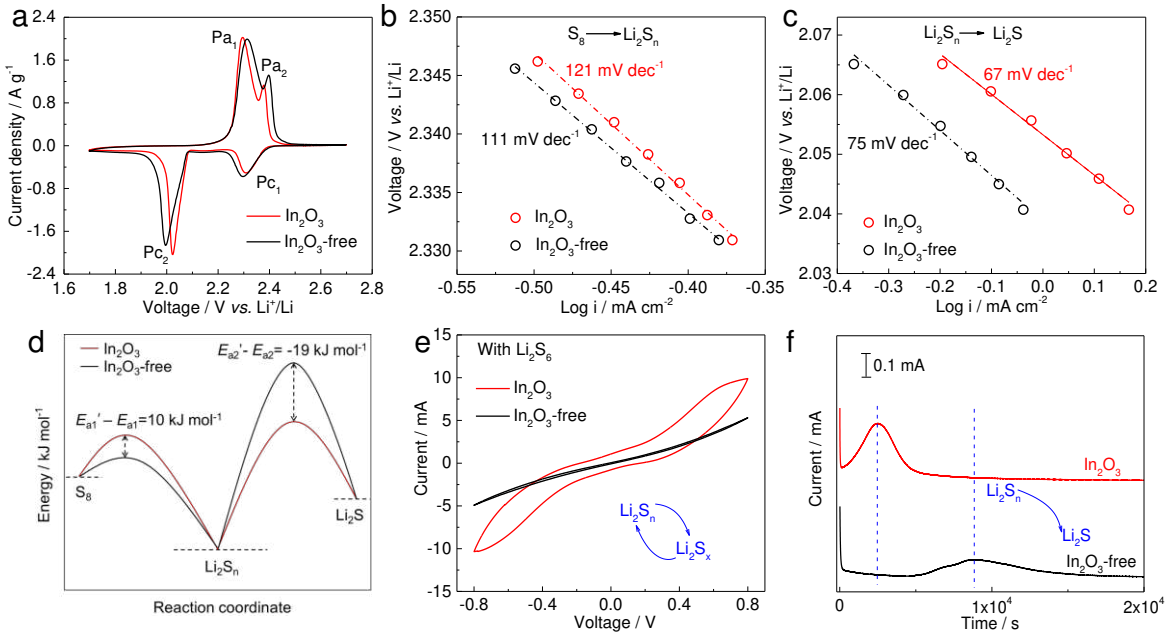

Figure 1. Electrochemical properties of In_2O_3-catalyzed cathode in comparison to the In_2O_3-free case. (a) the second cycle of CV profiles for the In_2O_3-catalyzed and In_2O_3-free Li-S cells at a low scan rate of 0.1 mV s^{-1} and (b, c) Tafel plots corresponding to the reductions of elemental sulfur to Li_2S_n and Li_2S_n to Li_2S; (d) the relative activation energies of the two sulfur cathodes, where the In_2O_3-catalyzed cathode shows a higher energy barrier for the conversion from S_8 to Li_2S_n, but a lower energy barrier for the Li_2S_n-to-Li_2S conversion, in comparison to the In_2O_3-free case; (e) CV curves of symmetric dummy cells using In_2O_3-catalyzed and In_2O_3-free electrodes at a rapid scan rate of 20 mV s^{-1}; (f) potentiostatic discharge curves of a Li_2S_8/tetraglyme solution at 2.05 V on the In_2O_3 catalyzed and In_2O_3-free electrodes.

Selective catalysis in the consecutive redox reaction. To evaluate the In_2O_3 catalyst for the Li-S batteries, the In_2O_3 NPs were hybridized with a porous carbon support composed of reduced graphene oxides (G) and carbon nanotubes (CNT), which yielded a In_2O_3-based cathode denoted In_2O_3-G-CNT/S (an optimized 2.8 wt% In_2O_3) accommodating ~70 wt% sulfur (see the preparation details in Supplementary Fig. 1-3 and Supplementary Note 1). For reference, the catalyst-free sample (G-CNT/S) was prepared with the same procedure except for the absence of In_2O_3. Cyclic voltammetry (CV) curves for the In_2O_3-catalyzed and In_2O_3-free cells were compared in Figure 1a that were respectively assembled by coupling In_2O_3-contained and In_2O_3-free cathodes with the referenced Li foil anodes. For

the discharge, the two cathodic (reduction) peaks (Pc_1, Pc_2) correspond to the reduction of elemental sulfur (S_8) to Li_2S_n and then to Li_2S, respectively. For the charge, two distinguishable anodic (oxidation) peaks (Pa_1, Pa_2) are observed, which are respectively attributed to the conversions from Li_2S to Li_2S_n, and finally to elemental sulfur (S_8).[27] When compared to that of In_2O_3-free case, the CV curve of the In_2O_3-catalyzed cell shows a definite positive shift of the cathodic peak and negative shift of the anodic peak (Supplementary Fig. 9 and Supplementary Table 1), indicating the catalytic activity of In_2O_3.[14, 15] Specially, the In_2O_3-catalyzed cell shows a slightly lower kinetic current than the In_2O_3-free cell for the dissolution from S_8 to Li_2S_n as observed by the Pc_1 peak in Figure 1a. By comparison, the Li_2S_n-to-Li_2S conversion is greatly enhanced due to the presence of catalyst, which is evidenced by the apparently larger current density of Pc_2. The different changes (reduced or enhanced) of the kinetic currents for various reaction steps concisely prove the selective catalysis during the discharge process.

The selective catalysis is further confirmed by the comparation of Tafel plots for In_2O_3-catalyzed and In_2O_3-free cells (Figures 1b, c). The reduction and oxidation overpotentials of Li_2S_n have been significantly decreased due to the introduction of the In_2O_3 catalyst (Figure 1c and Supplementary Fig. 10). Exchange current densities were calculated from the Tafel plots, which reflect the intrinsic electron transfer rate between electrode and electrolyte (Supplementary Table 1). The In_2O_3-catalyzed cell shows larger exchange current densities in both discharge and charge process, which are 6.02 and 0.20 mA cm^{-2} respectively, compared to those of In_2O_3-free case (3.29 and 0.16 mA cm^{-2}). The increase of exchange current densities indicates faster charge transfer induced by the In_2O_3 catalyst. The Tafel slope, which is an indicator for the kinetics of sulfur redox reactions, was further compared between In_2O_3-catalyzed and In_2O_3-free cells. Very interestingly, the In_2O_3-catalyzed cell shows the higher Tafel slope of 121 mV dec^{-1} for the S_8-to-Li_2S_n conversion than the In_2O_3-free case (111 mV dec^{-1}), while the lower Tafel slope of 67 mV dec^{-1} for the Li_2S_n-to-Li_2S conversion compared with the In_2O_3-free case (75 mV dec^{-1}), indicating the decreased solid-to-liquid conversion rate while accelerated liquid-to-solid conversion. The difference in activation energy (E_a) can be calculated from the exchange current densities (see details in Supplementary Note 2). As shown in Figure 1d, the E_a value for the reduction for S_8 to Li_2S_n is increased by 10 kJ mol^{-1} for the In_2O_3-catalyzed cell as compared to that for the In_2O_3-free case, also indicating that the formation rate of Li_2S_n slows down. In the following reaction step, the E_a value for the reduction of Li_2S_n to Li_2S is greatly decreased by 19 kJ mol^{-1} with the In_2O_3-catalyzed cell as compared to the In_2O_3-free case, increasing their conversion rate. The increase of the activation energy for the formation of Li_2S_n and the obvious decrease in the activation energy for the following reduction to Li_2S strongly support the proposed selective catalysis, where the dissolution of S_8 to Li_2S_n becomes more sluggish but the

conversion from Li_2S_n to Li_2S goes faster by using the In_2O_3 catalyst. For the charge, the E_a value for the oxidation of Li_2S to Li_2S_n is greatly decreased by 74 kJ mol^{-1} with In_2O_3 catalyst compared to that of the In_2O_3-free case, indicating accelerated conversion of the deposited Li_2S and a cleaned-up surface (Supplementary Note 2 and Supplementary Fig. 11). Besides, the In_2O_3-catalyzed cell shows the lower charge-transfer resistance (R_{ct}) as identified by the electrochemical impedance spectroscopy (EIS) data (Supplementary Fig. 12), suggesting an enhanced interfacial affinity towards Li_2S_n with the In_2O_3 catalyst.[28]

CV tests were further carried out for the symmetric dummy cells that were assembled by coupling two same In_2O_3-catalyzed electrodes with Li_2S_6 electrolyte (Figure 1e). As expected, the In_2O_3-catalyzed cell shows a much higher current density than the In_2O_3-free case even at a fast scan rate of 20 mV s^{-1}, indicating the ultrafast conversion of Li_2S_n.[28, 29] Potentiostatically Li_2S precipitation test is specially used for evaluating the Li_2S_n-to-Li_2S conversion with the In_2O_3 catalyst. The coin cells for the tests were assembled using In_2O_3-loaded or In_2O_3-free carbon fiber paper (CP) as the cathodes, Li foil as the anode, and a Li_2S_8/tetraglyme solution as the catholyte. As shown in Figure 1f, potentiostatic discharge profiles at 2.05 V were collected. The results show that the In_2O_3-catalyzed cell accelerates the Li_2S nucleation (~2500 s) compared with that free of In_2O_3. In addition, the Li_2S precipitate for the In_2O_3-catalyzed cell, which was evaluated based on the quantity of electric charge according to Faraday's law, shows a much higher capacity with a shorter nucleation time than those for the In_2O_3-free cell (Supplementary Fig. 13). Thus, Li_2S precipitation test gives a direct proof for the enhanced Li_2S_n-to-Li_2S conversion with the In_2O_3 catalyst.[28-31]

Battery performance. An In_2O_3-catalyzed battery was evaluated for rate and cycling performances in comparison to the In_2O_3-free battery also with an optimized 2.8 wt% In_2O_3 in the cathode, where the battery gave the highest capacity at various rates (Supplementary Fig. 3a). The rate performances of the Li-S batteries assembled by coupling In_2O_3-catalyzed or In_2O_3-free cathodes with a Li foil anode are shown in Figure 2a. With the catalyst, the battery achieves a high discharge capacity of 1427, 876, 773, 692 and 502 mAh g^{-1} at a rate of 0.2, 0.5, 1.0, 2.0 and 4.0 C, respectively, all of which are much higher than those for the In_2O_3-free batteries. When abruptly switching the rate from 4.0 C back to the initial rate of 0.2 C, the original capacity is largely recovered, indicating the excellent reversible capacity of the In_2O_3-catalyzed battery at various rates.[32, 33] The In_2O_3-catalyzed battery shows a lower voltage difference (ΔE =131 mV) which was calculated based on the charge plateau and discharge plateau in the third cycle, as compared to the ΔE value of 141 mV for the In_2O_3-free case.[27] Besides, the In_2O_3-catalyzed battery exhibits much lower potential barrier in the charging process, indicating the activation energy (E_a) of the Li_2S-to-Li_2S_n conversion is greatly reduced (Supplementary Fig.14), consistent with that obtained from Tafel plots. The charge-discharge

curves of the batteries at various current rates (0.2-4.0 C) are illustrated in Figure 2c and Supplementary Fig.15. Note that the typical two discharge plateaus of the In_2O_3-catalyzed battery are clearly seen even at a very high rate of 4.0 C, while the second plateau of the In_2O_3-free battery, corresponding to the conversion of Li_2S_n to Li_2S_2/Li_2S, disappears when cycled at this current.

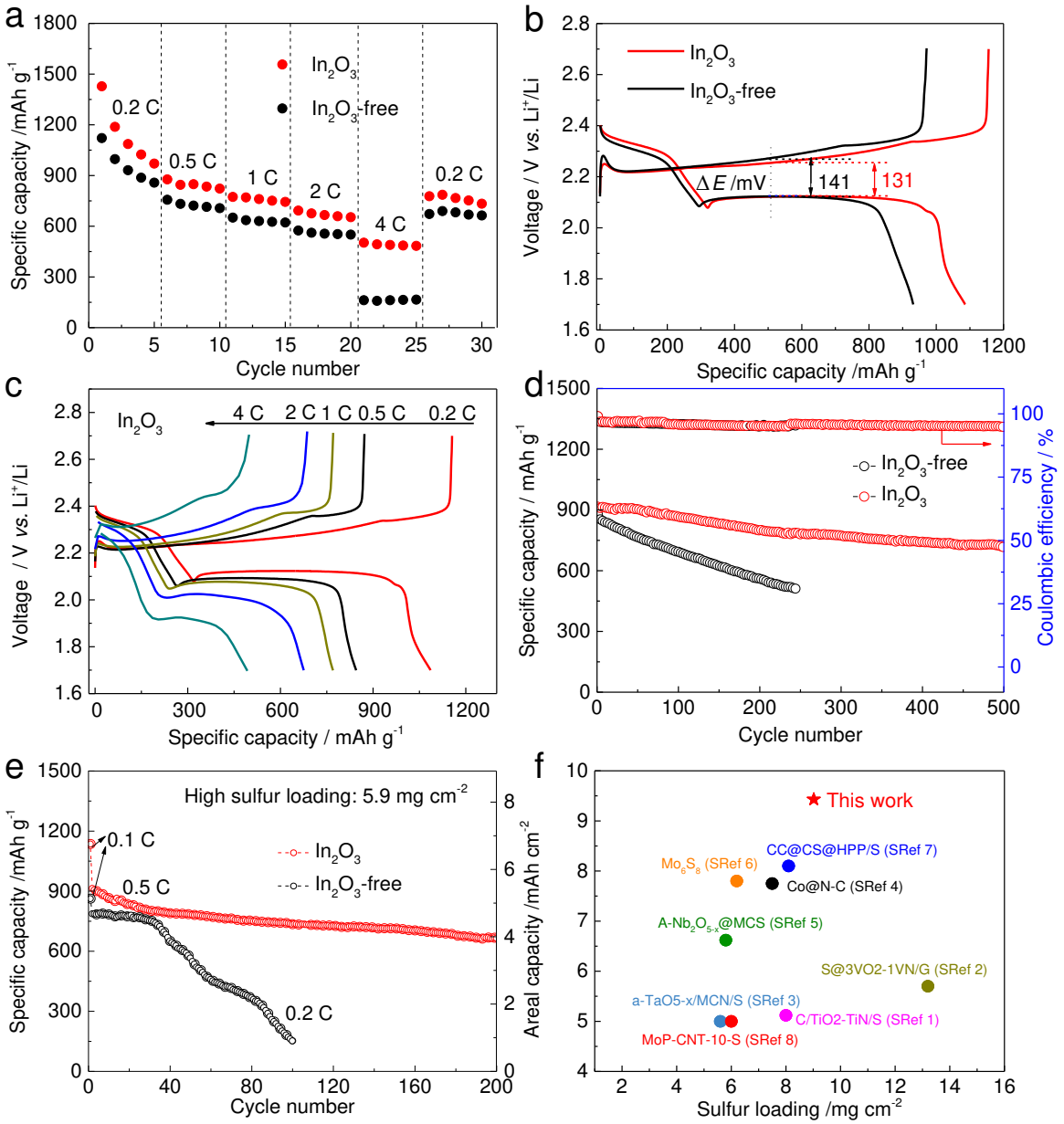

Figure 2. Electrochemical performance of In_2O_3-catalyzed Li-S battery in comparison to the In_2O_3-free battery. (a) rate performance (1C = 1675 mA g^{-1}); (b) galvanostatic discharge-charge profiles at 0.2 C; (c) galvanostatic charge-discharge profiles of the In_2O_3-catalyzed battery at various current rates; (d) cycling stability at 0.5 C; (e) cycling performance with a high sulfur mass loading of 5.9 mg cm^{-2} at 0.5 C and 0.2 C; (f) a comparison with other sulfur cathodes with electrolyte/sulfur ratios ≤ 8 μL/mg (SRef: Supplementary References).

The cycling performances were further compared at a 0.5 C as shown in Figure 2d. The In_2O_3-catalyzed battery exhibits superior capacity retention with stable coulombic efficiency. Specifically, it maintains a high capacity of 721 mAh g^{-1} after 500 cycles with a small capacity degradation of 0.04 % per cycle. In a sharp contrast, for the In_2O_3-free battery, the capacity quickly decays to 511 mAh g^{-1} with 0.17 % decay per cycle over 250 cycles. The excellent cycling performance of the In_2O_3-catalyzed cell indicates the great suppression of the shuttling effect.[18, 34] The SEM images (Supplementary Fig. 16 a-d) show that for the In_2O_3-catalyzed cell, the discharge products are homogeneously distributed at the surface after cycling at 0.5 C, while, for the In_2O_3-free case, the cracked and exposed filaments are seen.

The cathodes with high sulfur loadings were fabricated to evaluate the potential for practical applications.[35] The In_2O_3-catalyzed battery with a high sulfur areal loading up to 5.9 mg cm^{-2} delivers a higher initial capacity of 906 mAh g^{-1}, and a reversible capacity is maintained at 665 mAh g^{-1} with the retention of 73.4% over 200 cycles at 0.5 C; the initial capacity and its retention capability are much superior to those of the In_2O_3-free battery even at a current density of 0.2 C (Figure 2e). When the areal sulfur loading increases to 9.0 mg cm^{-2}, the In_2O_3-catalyzed battery displays a high initial areal capacity up to 9.4 mAh cm^{-2} (1046 mAh g^{-1}) at a current density of 0.9 mA cm^{-2} even with a low electrolyte/sulfur ratio (8 μL mg^{-1}); with an increased current density up to 1.8 mA cm^{-2}, the battery can be steadily cycled over 100 cycles with a reversible areal capacity of 5.3 mAh cm^{-2}, much higher than that of the commercial Li-ion batteries (~4.0 mAh cm^{-2}) (Supplementary Fig. 17).[33] The corresponding discharge plateaus are clearly seen even at such a high sulfur mass loading as shown in Supplementary Fig.18. In short, the areal capacities with high sulfur loadings are remarkable when compared to those for the reported sulfur hosts (Figure 2f and Supplementary Table 2). This excellent stability with high sulfur loadings strongly implies that the In_2O_3 nanocatalysts effectively prevent the accumulation of Li_2S_n in the electrolyte and decrease the need of electrolyte to some extent.[36]

Reaction pathway *in-situ* monitored by Raman spectroscopy. The Raman spectroscopy with 532 nm laser was employed to monitor the charge-discharge process of Li-S batteries with or without In_2O_3 catalyst. As shown in Figures 3a, b, for the discharge, the peaks located at 156, 223 and 476 cm^{-1} for elemental sulfur (S_8) and 134 and 310 cm^{-1} for In_2O_3 are detected at the open-circuit voltage (OCV) for the In_2O_3-catalyzed cell.[37, 38] Three characteristic peaks of S_8 remain until 2.04 V, indicative of strong adsorption of elemental sulfur on In_2O_3 and sluggish conversion to Li_2S_n. Upon the second plateau at 2.08 V a new peak at 398 cm^{-1} appears, attributed to the formation of Li_2S_n. When the voltage decreases to the end of the second plateau (~1.95 V), new peaks located at 448, 203 and 514 cm^{-1}

are detected, implying the change from S_6^{2-} to S_4^{2-}, then S_2^{2-} and Li_2S_2.[39, 40] Note that the Li_2S peak at 378 cm^{-1} is not

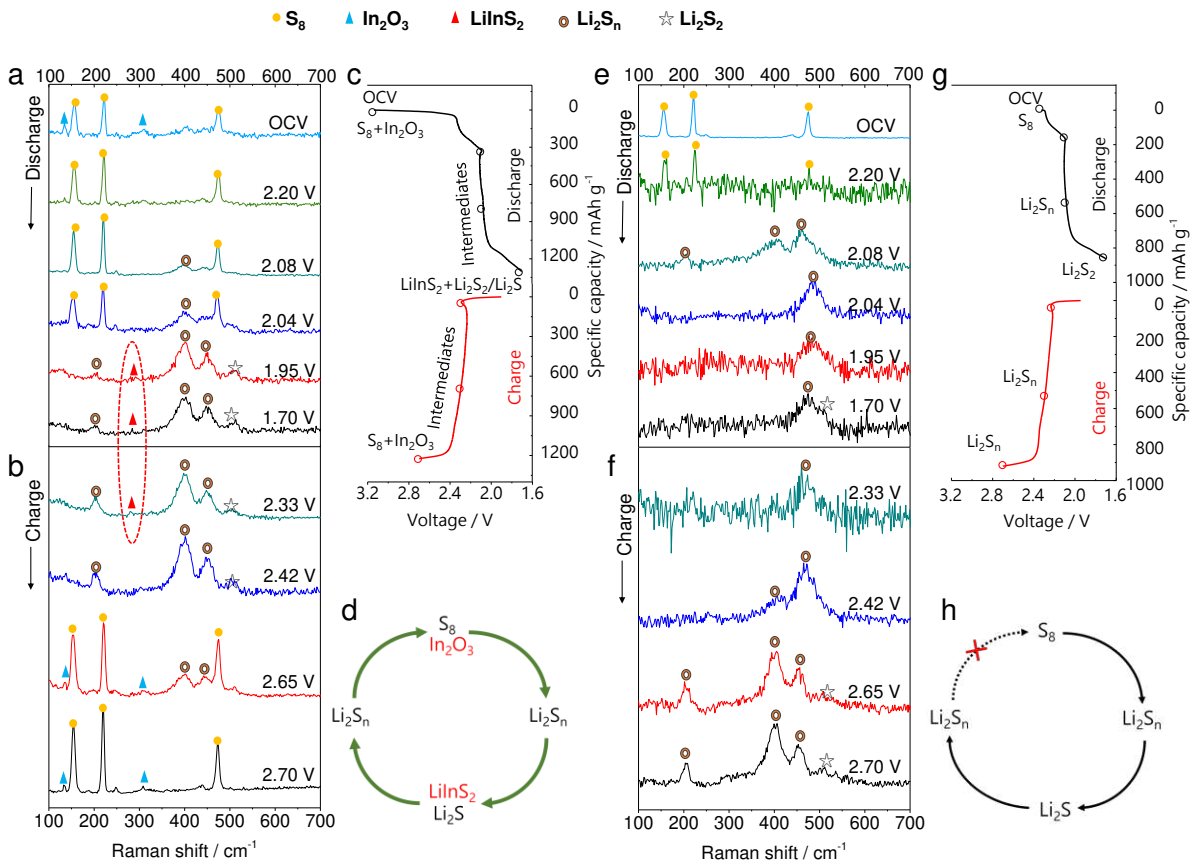

Figure 3. Reaction pathway demonstrated by *in-situ* Raman measurements. (a, b) Raman spectra of an In_2O_3-catalyzed battery and (c) the corresponding charge-discharge potentials of the detected substances; (d) a complete cycle of the sulfur redox with In_2O_3 catalyst; (e, f) Raman spectra of an In_2O_3-free battery and (g) the corresponding charge-discharge profile; (h) an incomplete cycle of the sulfur redox free of In_2O_3 catalyst. See more details in Supplementary Fig. 20.

detected even the Li-S cell was discharged to 1.7 V, which may be attributed to the sluggishness of solid state diffusion of Li ions and the signal is hard to be captured in the *in-situ* measurement.[41] Of interests, the peaks of In_2O_3 disappear before discharging to 1.95 V (Figure 3a and Supplementary Fig. 19), and a new peak at 284.7 cm^{-1} is then detected, which is due to a combination of stretching and torsion of S-In bonds and Li atom translational movements, probing the $LiInS_2$ intermediates involved in the catalytic process.[42] Comparatively, in the In_2O_3-free cell, Raman results (Figure 3e) indicate much faster conversion from S_8 to soluble Li_2S_n by demonstrating that the three characteristic peaks of elemental S were weakened at 2.20 V and totally disappeared at 2.08 V. However, it is hard to identify the solid discharge products even at 1.95 V for the In_2O_3-free battery; instead, the peaks for Li_2S_n are still maintained indicative of high concentrations of Li_2S_n in the electrolyte and a sluggish reduction to Li_2S. The sharp comparison for In_2O_3-catalyzed and In_2O_3-free cells well coincide with the above activation energy calculations obtained with the Tafel plots, which indicate, for the In_2O_3-catalyzed cell, the selective catalysis is well demonstrated in the

discharge process slowing down the S_8-to-Li_2S_n conversion with a higher energy barrier while accelerating the Li_2S_n-to-Li_2S conversion with a reduced energy barrier.

For the charge process (Figure 3b), the In_2O_3 catalyst with the probed $LiInS_2$ intermediates facilitates the Li_2S fast and full conversion to soluble Li_2S_n and eventually back to S_8 as the battery is charged to 2.70 V, completing a reaction cycle for sulfur redox reaction (Figures 3c, d); in a sharp contrast, this is hardly accomplished in In_2O_3-free cell under the same charge voltage and no S peaks are detected at 2.70 V (Figure 3 f). In the other words, without the catalyst, the battery cannot have a complete sulfur redox cycle upon charging to 2.70 V (Figures 3g, h). More informatively, for In_2O_3-catalyzed battery, the disappearance of the $LiInS_2$ intermediates, together with the re-detection of In_2O_3 peaks upon charging to 2.42 V, indicates that In_2O_3 catalyst is highly reversible in accompany with a fully cycled sulfur redox reaction, indicating $LiInS_2$ plays a crucial role in the catalysis in both discharge and charge processes.

We further combined the computational simulation to gain a better understanding on the formation of catalytic intermediates and the interaction between Li_2S_n and In_2O_3 in comparison to the clean graphene. To construct an accurate model of In_2O_3 catalyst, we have captured the annular dark-field scanning transmission electron microscopy (ADF-STEM) image as displayed in Figure 4a. It shows a lattice fringe with spacings of 1.79 and 2.92 Å, corresponding to the $(4\bar{4}4)$ and (222) plane of In_2O_3, respectively. The fast Fourier transforms (FFTs) agree with the ADF-STEM images (Figure 4b), which were taken along the [-1-12] zone axis. Therefore, In_2O_3 (222) surface was selected to optimize the geometries of Li_2S_n adsorption considering both of the ADF-STEM observations and XRD analysis (Supplementary Fig. 8). The result shows that Li_2S_4 tends to form In-S bonds with In on the In_2O_3 (222) surface and the In-S bond lengths (2.42, 2.61 Å) are close to that (2.49 Å) for the standard $LiInS_2$ (Figure 4c), which confirms the formation of the $LiInS_2$ intermediates. Figure 4d shows the 3D charge transfer maps between Li_2S_4 and In_2O_3 with an isosurface value of 2×10^{-3} e bohr^{-3}. Obvious charge accumulation is observed at the interface between S and In_2O_3, which indicates the strong interaction between In_2O_3 and Li_2S_n. To give a clear view on the charge transfer state, we constructed a 2D charge maps of In, S and O atoms in Figure 4e, where the yellow and blue regions suggest the negative and positive charges, respectively. There are obviously accumulated positive charges around the In atom, indicating that In atom tends to dissolve from the In_2O_3 lattice. Figure 4f shows the projected density of the state (PDOS) of the surface In 3*d* and S 2*p*. Obvious orbit overlapping of In *3d* and S *2p* is observed at the electron state around -2 eV below Fermi level, further confirming the interaction between In and S as well as the easy formation of $LiInS_2$ intermediates. Then, we investigated the binding energies between S_8 and the substrates (In_2O_3

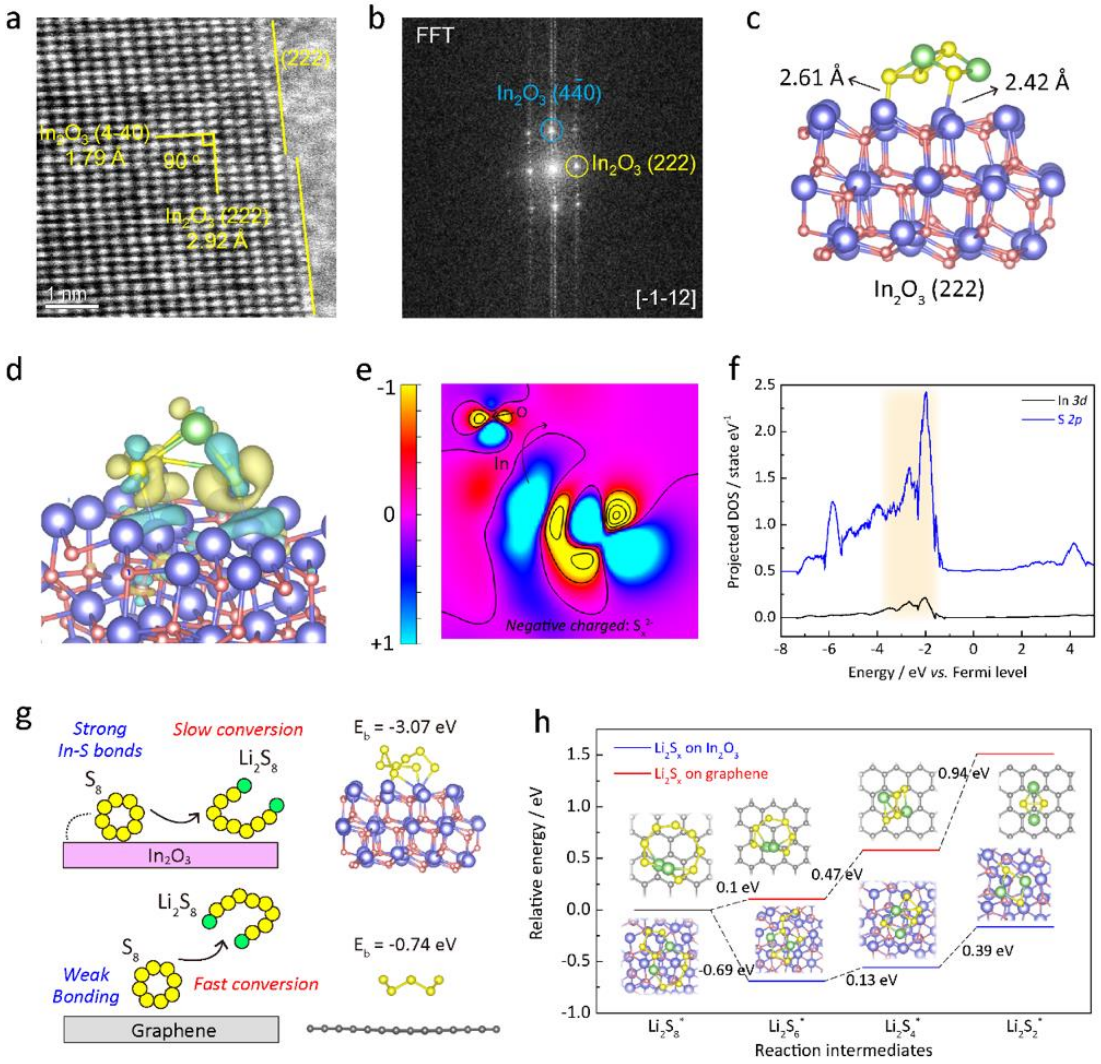

Figure 4. Computational simulation for the reaction pathway and $LiInS_2$ intermediate. (a) ADF-STEM image of the G-In_2O_3 hybrids; (b) the superimposed FFTs of In_2O_3; (c) the optimized structure of Li_2S_4 on In_2O_3 surface; The In-S bond length are 2.42 and 2.61 Å, which are very close to the standard In-S bond length in $LiInS_2$ (2.49 Å); (d) 3D charge difference of Li_2S_4 on In_2O_3; (e) 2D charge maps between In, O and S; (f) the projected DOS of In 3*d* and S 2*p*; (g) there is a much high binding energy of -3.07 eV between In_2O_3 and S_8, compared to that of -0.74 eV of clean graphene substrate. Hence, S_8 is hard to be desorbed from the In_2O_3 surface, and this slows down the conversion from S_8 to Li_2S_8; (h) the reaction pathway from $Li_2S_8^*$, $Li_2S_6^*$, $Li_2S_4^*$ to $Li_2S_2^*$ intermediates on the In_2O_3 and graphene substrates.

or clean graphene). As shown in Figure 4g, there is a much higher binding energy of -3.07 eV between In_2O_3 and S_8, compared to that of -0.74 eV of clean graphene substrate. Elemental sulfur (S_8) is easy to be adsorbed onto the In_2O_3 surface due to the higher binding energy resulting from the strong In-S bonds, which slows down the conversion from S_8 to Li_2S_8 to some extent. Finally, we build the reaction pathways by considering the $Li_2S_8^*$, $Li_2S_6^*$, $Li_2S_4^*$ and $Li_2S_2^*$ polysulfide intermediates (Figure 4h). As expected, the energy barrier for polysulfide conversion is greatly reduced

with the catalyst. For example, there is an obvious energy barrier of 0.47 eV for the conversion from $Li_2S_6^*$ to $Li_2S_4^*$ on the clean graphene substrate. In contrast, this conversion on the In_2O_3 catalyst is only 0.13 eV, confirming that the catalyst accelerates the redox conversions from the long-chain to short-chain polysulfides.

Reversible redox reaction with the $LiInS_2$ intermediates. The crystalline $LiInS_2$ was synthesized (see Experimental section) to further demonstrate how the intermediate works in the Li_2S_n conversion, and the XRD pattern (Figure 5a) confirms the orthorhombic $LiInS_2$ structure with a space group of Pna21 (the standard PDF #36-1352).[43] A $LiInS_2$-based battery was then assembled with the $LiInS_2$ loaded carbon paper (CP) coupled with a Li anode and Li_2S_8 catholyte. A $LiInS_2$-free battery for reference was assembled in the same way. Upon discharged to 2.1 V, two new peaks at 288 and 303 cm^{-1} due to the stretching and torsional movement of S-In bonds in $LiInS_2$ are detected by Raman spectroscopy except for the original characteristic peaks (Figure 5b).[42] These newly appearing peaks have similar positions to that of $LiInS_2$ detected in *in-situ* Raman measurement for In_2O_3-catalyzed battery as shown in Figure 3a. As expected, it is hard to probe Li_2S_n in the Raman spectrum for the $LiInS_2$-based battery, indicating the greatly accelerated Li_2S_n conversion with the $LiInS_2$. It is reasonable that no $LiInS_2$ peaks are observed for the $LiInS_2$-free battery from 260 to 310 cm^{-1}, and the peaks corresponding to the Li_2S_n at 398, 448 and 533 cm^{-1} are detected, indicating the sluggish conversion. The above results confirm the critical role of $LiInS_2$ intermediates in the fast conversion of Li_2S_n.

The evolution of the $LiInS_2$ intermediate can be also demonstrated by the X-ray photoelectron spectra (XPS) spectra at the fully discharged state of the In_2O_3-catalyzed cathode. The In 3d core-level XPS spectrum for the fresh cathode shows typical doublets at 445.0 and 452.6 eV for In_2O_3. After complete discharge, two additional signals at 445.2 and 452.8 eV are detected, which are possibly attributed to the binding of In-S in $LiInS_2$ when compared to the XPS spectrum for pure $LiInS_2$ (Figure 5c). In addition, the doublets for the S 2p core bands of the discharged In_2O_3-catalyzed cathode can be deconvoluted into four phases; the signals at 169.0, 170.0 eV and 167.1, 168.1eV fitted can be assigned to sulfate and sulfite, and the relatively weak peaks can be attributed to Li_2S and the $LiInS_2$ intermediate, respectively.

The ADF-STEM images with line scan elemental maps were used to characterize the In_2O_3-catalyzed cell before and after charging. The comparison of the cases for the fresh (Fig. 5f) and the fully charged (Fig. 5g) In_2O_3-catalyzed cells show that sulfur is enriched at the In_2O_3 surface for the fully charged case, which coincide well with the *in-situ* Raman results suggesting that sulfur is completely converted back to crystalline S. In addition, according to the XPS results (Figure 5d), the disappearance of Li_2S peak (160.0 eV, 161.0 eV) together with the appearance of S peak

(164.2 eV, 165.2 eV) at the fully charged state confirm high reversibility of the sulfur species during the discharge-charge cycle. In a sharp contrast, Li_2S peaks were detected both in the discharged and charged states from the In_2O_3-free cell (Figure 5e) suggesting poor reversibility of the insoluble discharge products.[14] In short, both active sulfur and In_2O_3 catalysts are fully reversible, and the In_2O_3 catalyst together with the $LiInS_2$ intermediates plays a crucial role in accelerating Li_2S_n conversion and specially in the charge process, fully converts them into elemental sulfur.

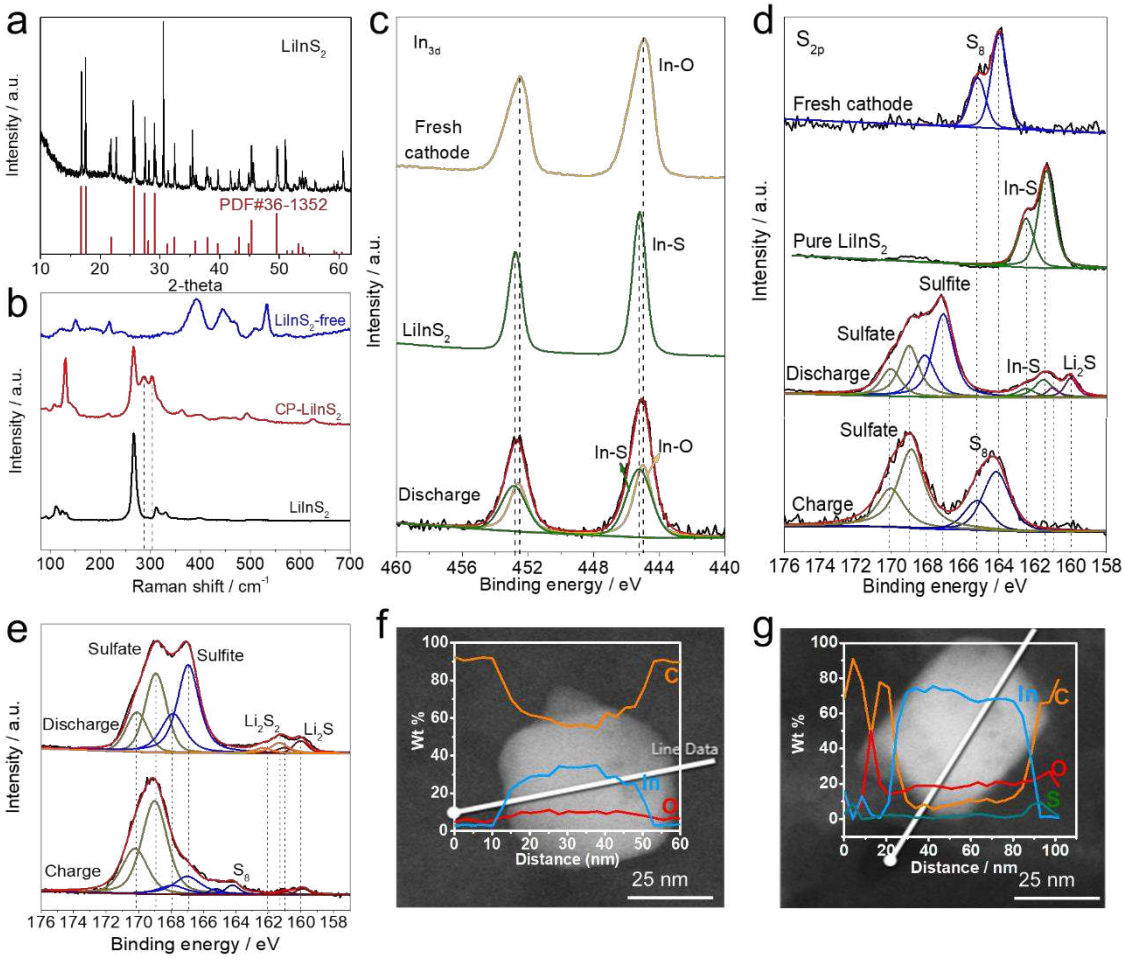

Figure 5. Conversion of polysulfide (Li_2S_n) with $LiInS_2$ as a catalysis intermediate. (a) XRD patterns of the prepared $LiInS_2$; (b) Raman spectra (irradiated with 532 nm laser) of the synthesized $LiInS_2$, $LiInS_2$-free and $LiInS_2$-based cathode (CP-$LiInS_2$) discharged at 2.1 V; (c) XPS spectra for the 3d level of In: pristine In_2O_3, prepared $LiInS_2$ and the In_2O_3 cathode in the fully discharged state; (d) S_{2p} XPS spectra of fresh cathode, pure $LiInS_2$ and the In_2O_3-catalyzed cathode in the fully discharged and charged state; (e) S_{2p} XPS spectra of the In_2O_3-free cathode in the fully discharged and charged state; ADF-STEM images and corresponding line scan elemental mapping of (f) fresh In_2O_3 and (g) the In_2O_3-catalyzed cathode in the fully charged state.

Understanding of deactivation of the In_2O_3 catalysts. To gain insight on the stability of In_2O_3 nanocatalyst, a critical operation condition was carried out that is a long run battery test at an ultrahigh rate of 4.0 C. As shown in Figure 6a and Supplementary Fig. 21, the In_2O_3-catalyzed battery demonstrates outstanding stability with negligible

capacity decay up to 1000 cycles. Unfortunately, the battery is then presented capacity decay (Supplementary Fig. 22), which implies the deactivation of In_2O_3 nanocatalyst due to the surface "poising". Figure 6b shows the S 2p XPS spectra of In_2O_3-catalyzed cathode after the first cycle of discharge. As expected, the S 2p core level bands for the discharge product Li_2S and the $LiInS_2$ intermediates (In-S bond) are obviously detected on the catalyst surface, indicative of a fast conversion of Li_2S_n in presence of $LiInS_2$. In a sharp contrast, the S 2p core level bands for Li_2S and $LiInS_2$ (In-S bond) are undetected in the cathode over 1000 cycles of discharge. Instead, the signals at 163.5 and 164.5 eV corresponding to the S 2p core level bands for accumulated Li_2S_n were detected (Figure 6b), suggesting that most of Li_2S_n are not converted into Li_2S. The high coverage of In_2O_3 particles with the irreversible sulfate (excess oxidation product, see Supplementary Fig. 16 e, f) is the possible reason to inhibit the formation of $LiInS_2$ intermediates, thereby resulting in deactivation of the catalyst and the slow conversion of Li_2S_n to Li_2S. In fact, the high coverage of strong adsorbate on the surface is a general reason for deactivation of a solid catalyst in a S-containing reaction, [44] which indicates, in spite of accelerated conversion of Li_2S_n to Li_2S, the catalyst poising is still an important issue to overcome for the design of high-performance catalyst for Li-S batteries.

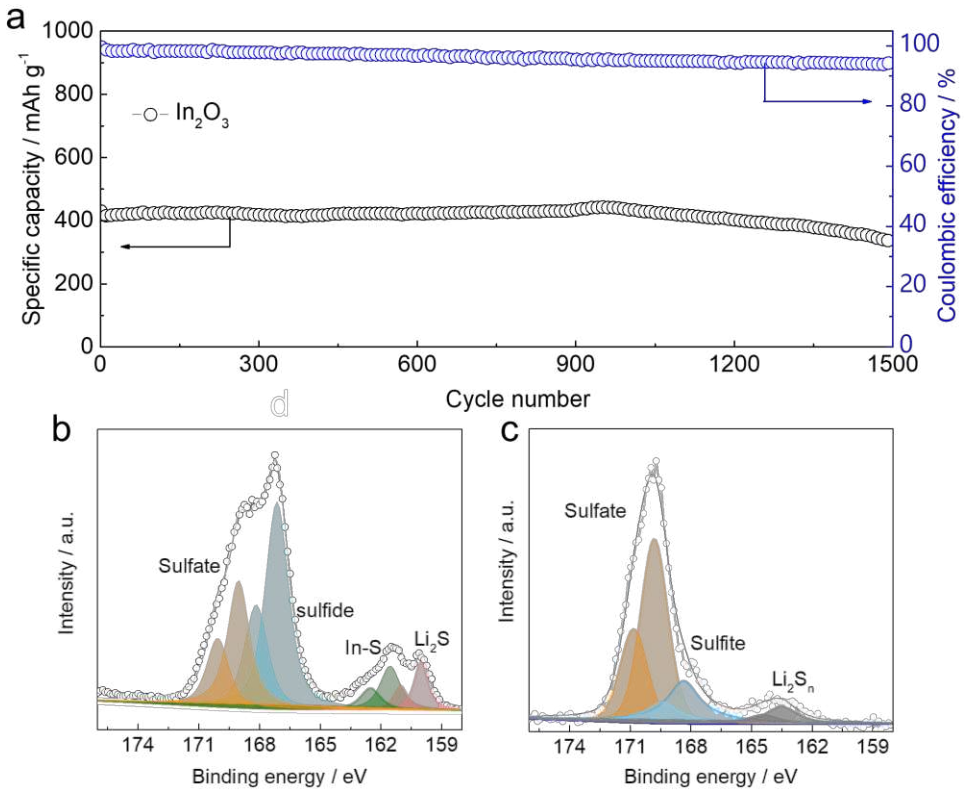

Figure 6. The deactivation of In_2O_3 catalyst. (a) cycling performance of In_2O_3-catalyzed battery at 4.0 C with a catalyst deactivation over 1000 cycles; S_{2p} XPS spectra of In_2O_3-catalyzed cathode for the 1st (b) and 1000th cycle (b) in the fully discharged states.

Discussion

We propose the selective catalysis as a remedy for the shuttle effect for Li-S batteries. Targeting at different steps in the consecutive solid-liquid-solid reaction, the proof-of-concept catalyst, In_2O_3, slows down the solid-liquid reaction, dissolution of elemental sulfur to soluble Li_2S_n while accelerates the liquid-solid reaction, deposition of Li_2S_n into insoluble discharge product Li_2S/Li_2S_2, which basically reduces the accumulation of soluble polysulfide in the electrolyte and represents a root solution for tackling the shuttle effect. The selective catalysis is featured by the changes of activation energies (*E*a) and kinetic currents in the consecutive redox reaction, modified reaction pathway together with the probed $LiInS_2$ intermediates demonstrated by the *in-situ* Raman spectra, as well as the catalyst deactivation after 1000 cycles. The $LiInS_2$ intermediates probed by experimental study and computational simulation has been proved to accelerate the SRR and SER, and especially, substantially promote the conversion from Li_2S to Li_2S_n, and finally to elemental sulfur, increasing the conversion. As a result, the Li-S batteries work steadily with negligible capacity decay over 1000 cycles at an ultrahigh rate of 4.0 C. Moreover, with a high areal sulfur loading (~9.0 mg cm^{-2}) yet a low electrolyte/sulfur ratio (8 μL mg^{-1}), the battery still displays a high initial areal capacity up to 9.4 mAh cm^{-2} at a current density of 0.9 mA cm^{-2}. This work featured with selective catalysis, we hope, provides a valuable inspiration for the rational design of catalysts in Li-S batteries and finally accelerates the practical use and commercialization of Li-S batteries by basically suppressing the loss of active sulfur and reducing the amount of required electrolyte.

Methods

Synthesis of CNT/S composites. The carbon nanotube/sulfur composites (CNT/S) were prepared by a simple melt-diffusion method.[27] In a typical procedure, the CNTs and sulfur (99.99% pure metal basis, Aladdin) were mixed in the desired ratio. Then the powder was grounded and heated under an ambient atmosphere at 155 °C for 12 h.

Synthesis of the GO-In_2O_3 composites. Graphite oxide (GO) was synthesized from natural graphite by a modified Hummers method as reported previously.[45] Commercial In_2O_3 NPs and a graphene oxide suspension (6.5 mg mL^{-1}) with the precalculated target compositions were dispersed in the water ethanol mixtures and a homogenized GO-In_2O_3 (2.0 mg mL^{-1}) liquid was formed by sonication for 2 h.

Synthesis of In_2O_3-G-CNT/S, G-CNT/S, and G-In_2O_3 composites. The homogenized GO-In_2O_3 (2.0 mg mL^{-1}) suspension was added to the CNT/S composites under continuous ultrasonication and then a certain amount of L-ascorbic acid sodium salt as the reducing agent was added to the solution. The mixture was transferred to a sealed glass bottle, which was heated to 70 °C for 24 h. The prepared

sample was rinsed with deionized water several times and a stiff rod-like In_2O_3-G-CNT/S composite was formed after drying. G-CNT/S and G-In_2O_3 composites were synthesized using a similar process to that for the In_2O_3-G-CNT/S composite without adding In_2O_3 or a CNT/S composite.

Assembly of symmetric dummy cells. Li_2S and S in amounts corresponding to the nominal stoichiometry of Li_2S_6 were added to a 1: 1 (v/v) DOL/DME mixture and stirred overnight at 50 °C. The concentration of the Li_2S_6 solution prepared was 0.1 mol L^{-1}. The CP was punched into small disks with a diameter of 10.0 mm. 0.3 mg cm^{-2} G-In_2O_3 and graphene powders was loaded onto CP disks and were denoted as In_2O_3-based and In_2O_3-free electrodes, respectively. The typical loading procedure involved a sequence of ultrasonic dispersing In_2O_3-based powders in NMP, dropwise adding the suspension onto CP disks, and then drying the electrodes at 55 ºC for 12.0 h. Two identical electrodes were assembled into a standard 2032 coin cell, and 20.0 μL Li_2S_6 electrolyte was added.

Cell assembly and electrochemical measurements. The In_2O_3-based cathodes were prepared by mixing In_2O_3-G-CNT/S powder (95 wt%) and poly (vinylidene fluoride) (5 wt%) as a binder dissolved in N-methyl-2-pyrrolidone (NMP) to form a slurry, which was then coated onto an Al foil and vacuum-dried at 55 °C for 12 h. For reference, we also fabricated In_2O_3-free cathodes with G-CNT/S powder. The foil was then cut into a circle of diameter 10 mm for use as the cathode. CR2032 coin cells were assembled using the coated Al foil as the current collector for cathode, a lithium metal foil anode, Celgard 2400 as the separator, and 1.0 M lithium bis-trifluoromethanesulphonylimide (LiTFSI) dissolved in 1, 3-dioxolane and 1, 2-dimethoxyethane (DOL: DME, 1:1 vol) with 1.0 wt% $LiNO_3$ additive as the electrolyte. The electrolyte/sulfur ratios were about 20, 10 and 8 μL mg^{-1} for the electrodes with sulfur loadings of 1.0, 5.9 and 9.0 mg cm^{-2}, respectively.

The galvanostatic discharge/charge measurements were conducted using a Neware battery test system. The cathode specific capacities were normalized only by the mass of sulfur, as per common practice. The charge-discharge voltage range was 1.7–2.7 V (vs. Li^+/Li). CV curves were obtained using an Autolab workstation at a scan rate of 0.1 mV s^{-1} with a potential range of 1.7–2.7 V (vs. Li^+/Li) and EIS was conducted using an Autolab workstation with a frequency range of 0.01–10^5 Hz.

Measurement for the nucleation of lithium sulfide (Li_2S). A Li_2S_8 solution (0.2 mol L^{-1}) was used as the electrolyte and was prepared by combining stoichiometric amounts of lithium sulfide and sulfur powder in tetraglyme under vigorous magnetic stirring. The CP was punched into circular disks with diameters of 10 mm and used as the current collector to load 0.3 mg G or G-In_2O_3 powders for cell assembly and a lithium foil was used as the anode. 20 μl Li_2S_8 electrolyte was first distributed in the cathode and then 20 μl of the electrolyte without Li_2S_8 was dropped onto the lithium anode compartment. The assembled cells were first discharged galvanostatically at 0.112 mA to 2.06 V and then discharged potentiostatically at 2.05 V for Li_2S nucleation and growth. The potentiostatic discharge was terminated when the current fell below 10^{-5} A.[23]

Synthesis of the crystalline $LiInS_2$. The commercial LiF (98+%, Alfa) and In_2S_3 (99.99% metal basis, Aladdin) were mixed with a molar ratio of 2:1. Then the powder was grounded and heated under vacuum atmosphere at 750 °C for 5 h and cooled at room temperature to obtain the crystalline $LiInS_2$.

CP-$LiInS_2$ Cell assembly. The CP was punched into circular disks with diameters of 10 mm and used as the current collector to load

1.0 mg $LiInS_2$ powders for cell assembly and a lithium foil was used as the anode. 20 μl Li_2S_8 electrolyte was first distributed in the cathode and then 20 μl of the electrolyte without Li_2S_8 was dropped onto the lithium anode compartment. $LiInS_2$-free cell was assembled as the same procedure using the CP as the current collector without $LiInS_2$ powders.

***In-Situ* Raman Spectroscopy.** Li-S coin cells with a quartz window and a hole on the stainless steel were used for the in-situ Raman spectroscopy analysis at 532 nm Laser (Supplementary Fig 23). The sulfur cathodes were prepared by mixing In_2O_3-based/free powder (95 wt%) and poly tetra fluoroethylene (5 wt%) dissolved in ethanol as a binder to form a self-supporting electrode and vacuum-dried at 55 °C for 12 h. The cells were tested at a rate of 0.05 C.

Computational Section. All calculations in this work were carried out using density functional theory (DFT) method as implemented in the VASP code. The electronic exchange-correlation energy was modeled using the Perdew-Burke-Ernzerhof (PBE) functional within the generalized gradient approximation (GGA). The projector augmented wave (PAW) method was used to describe the ionic cores. For the plane-wave expansion, a 450 eV kinetic energy cut-off was used after testing a series of different cut-off energies. A Monkhorst-Pack 3×3×1 k-point grid was used to sample the Brillouin zone. The convergence criterion for the electronic structure iteration was set to be 10^{-4} eV, and that for geometry optimizations was set to be 0.01 eV $Å^{-1}$ on force. A Gaussian smearing of 0.1 eV was applied during the geometry optimization and for the total energy computations. For the density of states (DOS) computations, a tetrahedron method with Blöchl correction was employed. Denser k-points (5×5×1) were used to improve the quality of DOS computations. The projected DOS patterns were extracted from the total DOS results.

Structural Characterization. SEM was performed on a Hitachi S4800 (Hitachi Japan) instrument. ADF-STEM measurements were conducted on a Hitachi HF5000 coupled with an energy dispersive spectrometer (EDS). The Raman spectra were recorded on a MicroRaman system (LabRAM HR spectrometer, Horiba) with an Olympus BX microscope and an argon ion laser (532 nm). XRD patterns were collected on a Bruker D-8 diffractometer (Cu Kα radiation, $\lambda = 0.154$ nm) at room temperature. TG (Rigaku, Japan) was performed in air from room temperature to 500 °C at a heating rate of 10 °C per minute to calculate the amount of sulfur in the hybrids. Nitrogen adsorption measurement was conducted at 77 K using a BEL-mini instrument (BEL Inc., Japan). The specific surface area was obtained by Brunauer–Emmett–Teller (BET) analysis of the adsorption isotherm. XPS data were recorded by an ESCALAB 250Xi (Thermo Fisher) with a monochromatic Al Ka source to analyze the surface species and their chemical states.

Data availability

The data supporting the findings of this work are available within the article and its Supplementary Information files. All other relevant data supporting the findings of this study are available from the corresponding author on request.

References

1. Bruce PG, Freunberger SA, Hardwick LJ, Tarascon JM. Li-O_2 and Li-S batteries with high energy storage. *Nature Mater.***11**, 19-29 (2011).

2. Peng Q, et al. Advances in lithium–sulfur batteries based on multifunctional cathodes and electrolytes. *Nat. Energy* **1**,16132 (2016).

3. Fang R, Zhao S, Sun Z, Wang DW, Cheng HM, Li F. More Reliable Lithium-Sulfur Batteries: Status, Solutions, and Prospects. *Adv. Mater.* **29**, 1606823 (2017).

4. Bhargav A, He J, Gupta A, Manthiram A. Lithium-Sulfur Batteries: Attaining the Critical Metrics. *Joule* **4**, 285-291 (2020).

5. Bai S, Liu X, Zhu K, Wu S, Zhou H. Metal-organic framework-based separator for lithium-sulfur batteries. *Nat. Energy* **1**,16094 (2016).

6. Xue W, et al. Intercalation-conversion hybrid cathodes enabling Li–S full-cell architectures with jointly superior gravimetric and volumetric energy densities. *Nat. Energy* **4**, 374-382 (2019).

7. Ji X, Lee KT, Nazar LF. A highly ordered nanostructured carbon-sulphur cathode for lithium-sulphur batteries. *Nature Mater.* 8, 500-506 (2009).

8. Pei F, et al. Self-supporting sulfur cathodes enabled by two-dimensional carbon yolk-shell nanosheets for high-energy-density lithium-sulfur batteries. *Nat. Commun.* 8, 482 (2017).

9. Tao X, et al. Balancing surface adsorption and diffusion of lithium-polysulfides on nonconductive oxides for lithium-sulfur battery design. *Nat. Commun.* 7, 11203 (2016).

10. Yang A, et al. Electrochemical generation of liquid and solid sulfur on two-dimensional layered materials with distinct areal capacities. *Nature Nanotech.* **15**, 231-237 (2020).

11. Li G, et al. Chemisorption of polysulfides through redox reactions with organic molecules for lithium-sulfur batteries. *Nat. Commun.* **9**, 705 (2018).

12. Zhang J, et al. Double-Shelled Nanocages with Cobalt Hydroxide Inner Shell and Layered Double Hydroxides Outer Shell as High-Efficiency Polysulfide Mediator for Lithium-Sulfur Batteries. *Angew. Chem., Int. Ed.* **55**, 3982-6 (2016).

13. Guo L, et al. Enhanced Multiple Anchoring and Catalytic Conversion of Polysulfides by Amorphous MoS_3 Nanoboxes for High-Performance Li-S Batteries. *Angew. Chem., Int. Ed.* **59**, 13071-13078 (2020).

14. Al Salem H, Babu G, Rao CV, Arava LM. Electrocatalytic Polysulfide Traps for Controlling Redox Shuttle Process of Li-S Batteries. *J. Am. Chem. Soc.* **137**, 11542-11545 (2015).

15. Liu D, et al. Catalytic Effects in Lithium-Sulfur Batteries: Promoted Sulfur Transformation and Reduced Shuttle Effect. *Adv. Sci.* **5**, 1700270 (2018).

16. Zhou G, et al. Catalytic oxidation of Li_2S on the surface of metal sulfides for Li-S batteries. Proc. Natl. Acad. Sci. U. S. A. 114, 840-845 (2017).

17. Chen T, et al. Self-Templated Formation of Interlaced Carbon Nanotubes Threaded Hollow Co_3S_4 Nanoboxes for High-Rate and Heat-Resistant Lithium-Sulfur Batteries. *J. Am. Chem. Soc.* **139**, 12710-12715 (2017).

18. Wang R, et al. Bidirectional Catalysts for Liquid-Solid Redox Conversion in Lithium-Sulfur Batteries. *Adv. Mater.* 2000315 (2020).

19. Zhao M, et al. Activating Inert Metallic Compounds for High-Rate Lithium–Sulfur Batteries Through In Situ Etching of Extrinsic Metal. *Angew. Chem. Int. Ed.* **58**, 3779 –3783 (2019).

20. Sun Z, et al. Conductive porous vanadium nitride/graphene composite as chemical anchor of polysulfides for lithium-sulfur batteries. *Nat. Commun.* **8**, 14627 (2017).

21. Wang J, et al. Double-Shelled Phosphorus and Nitrogen Codoped Carbon Nanospheres as Effcient Polysulfde Mediator for High Performance Lithium–Sulfur Batteries. *Adv. Sci.* **5**, 1800621 (2018).

22. Zhou J, et al. Deciphering the Modulation Essence of p Bands in Co-Based Compounds on Li-S Chemistry. *Joule* **2**, 2681-2693 (2018).

23. Zhong Y, et al. Surface Chemistry in Cobalt Phosphide-Stabilized Lithium-Sulfur Batteries. *J. Am. Chem. Soc.* **140**, 1455-1459 (2018).

24. Chao Y, et al. 2D MoN-VN Heterostructure To Regulate Polysulfides for Highly Efficient Lithium-Sulfur Batteries. *Angew. Chem. Int. Ed.* **57**, 16703-16707 (2018).

25. Zhou T, et al. Twinborn TiO_2-TiN heterostructures enabling smooth trapping–diffusion–conversion of polysulfides towards ultralong life lithium-sulfur batteries. *Energy Environ. Sci.* **10**, 1694-1703 (2017).

26. Peng L, et al. A fundamental look at electrocatalytic sulfur reduction reaction. *Nature Catalysis*, **3**, 762-770 (2020).

27. Zheng C, et al. Propelling polysulfides transformation for high-rate and long-life lithium-sulfur batteries. *Nano Energy* **33**, 306-312 (2017).

28. Peng HJ, et al. Enhanced Electrochemical Kinetics on Conductive Polar Mediators for Lithium-Sulfur Batteries. *Angew. Chem., Int. Ed.* **55**, 12990-12995 (2016).

29. Ye Z, Jiang Y, Li L, Wu F, Chen R. A High-Efficiency CoSe Electrocatalyst with Hierarchical Porous Polyhedron Nanoarchitecture for Accelerating Polysulfides Conversion in Li-S Batteries. *Adv. Mater.* **32**, 2002168 (2020).

30. Yuan H, et al. Conductive and Catalytic Triple-Phase Interfaces Enabling Uniform Nucleation in High-Rate

Lithium-Sulfur Batteries. *Adv. Energy Mater.* **9**, 1802768 (2019).

31. Song Y, et al. Synchronous immobilization and conversion of polysulfides on a VO_2–VN binary host targeting high sulfur load Li–S batteries. *Energy Environ. Sci.* **11**, 2620-2630 (2018).

32. Pei F, et al. Self-supporting sulfur cathodes enabled by two-dimensional carbon yolk-shell nanosheets for high-energy-density lithium-sulfur batteries. *Nat. Commun.* 8, 482 (2017).

33. Fang R, et al. Single-wall carbon nanotube network-enabled ultrahigh sulfur-content electrodes for high-performance lithium-sulfur batteries. *Nano Energy* **42**, 205-214 (2017).

34. Zhou G, et al. Theoretical Calculation Guided Design of Single-Atom Catalysts toward Fast Kinetic and Long-Life Li-S Batteries. Nano Lett. **20**, 1252-1261(2020).

35. Jiao L, et al. Capture and Catalytic Conversion of Polysulfides by In Situ Built TiO_2 - MXene Heterostructures for Lithium-Sulfur Batteries. *Adv. Energy Mater.* **9**. 1900219 (2019).

36. Zhao M, Li BQ, Peng HJ, Yuan H, Wei JY, Huang JQ. Lithium-Sulfur Batteries under Lean Electrolyte Conditions: Challenges and Opportunities. *Angew. Chem., Int. Ed*, **59**, 2-19 (2020).

37. Zhang L, et al. In situ optical spectroscopy characterization for optimal design of lithium-sulfur batteries. *Chem. Soc. Rev.* **48**, 5432-5453 (2019).

38. Meng L, Rao D, Tian W, Cao F, Yan X, Li L. Simultaneous Manipulation of O-Doping and Metal Vacancy in Atomically Thin Zn10In16S34 Nanosheet Arrays toward Improved Photoelectrochemical Performance. *Angew. Chem., Int. Ed.* **57**, 16882-16887 (2018).

39. Chen W, et al. A New Hydrophilic Binder Enabling Strongly Anchoring Polysulfides for High-Performance Sulfur Electrodes in Lithium-Sulfur Battery. *Adv. Energy Mater.* **8**, 1702889 (2018).

40. Hagen M, et al. In-Situ Raman Investigation of Polysulfide Formation in Li-S Cells. *J. Electrochem. Soc.* **160**, A1205-A1214 (2013).

41. Yeon J-T, Jang J-Y, Han J-G, Cho J, Lee KT, Choi N-S. Raman Spectroscopic and X-ray Diffraction Studies of Sulfur Composite Electrodes during Discharge and Charge. *J. Electrochem. Soc.* **159**, A1308-A1314 (2012).

42. Ma T, Sun L, Xu C, Chen Y. First-principles study of lattice dynamics and thermodynamic properties of $LiInX_2$ (X=S, Se, Te). *J. Alloys Compd.* **509**, 9733-9741 (2011).

43. Magesh M, Vijayakumar P, Arunkumar A, Anandha Babu G, Ramasamy P. Investigation of structural and optical properties in $LiInS_2$ single crystal grown by Bridgman-Stockbarger method for mid IR laser application. *Mater. Chem.Phys.* **149**, 224-229 (2015).

44. Kolpin A, et al. Quantitative Differences in Sulfur Poisoning Phenomena over Ruthenium and Palladium: An Attempt to Deconvolute Geometric and Electronic Poisoning Effects Using Model Catalysts. *ACS Catalysis* **7**, 592-605 (2016).

45. Lv W, et al. Low-Temperature Exfoliated Graphenes: Vacuum-Promoted Exfoliation and Electrochemical Energy Storage. *ACS Nano* **3**, 3730-3736 (2009).

Acknowledgements

We appreciate support from the National Natural Science Foundation of China (Nos. 51932005 and 21773156), the National Science Fund for Distinguished Young Scholars, China (No. 51525204), the Ministry of Education of China (PCSIRT_IRT_16R49), the Shanghai Sci. & Tech. and Edu. Committee (19070502700), the National Science Foundation of Tianjin, China (No. 18JCQNJC02300) and the National Key Research and Development Program of China (2018YFE0124500). We sincerely thank Drs. Y. M. Niu and H. Matsumoto for the ADF-STEM measurements and analysis.

Author contributions

Y. W and Q.-H.Y. conceived and supervised the research; W. H. and H. L. designed the experiment and W. H. carried out most of the experiments; H. L. was mainly responsible for the theoretical calculation; C. P. conducted the catalysis mechanism discussion including the activation energy evaluation. J. X. and Y. S. helped with material characterizations and analyzed the results; Y. J. helped with the DFT calculation and the related result discussion; B. Z. helped with the TEM measurements and related analyses. C. Z., W. L., Y. T., and S.-Z. Q. discussed the data and provided the technical support. Q.-H. Y., Y. W., W. H., and H. L. were preparing the manuscript with further inputs from other authors. All authors discussed the results and commented on the manuscript.

Additional information

Supplementary Information accompanies this paper at http://www.nature.com/reprints.

Competing interests: The authors declare no competing financial interests.

Figures

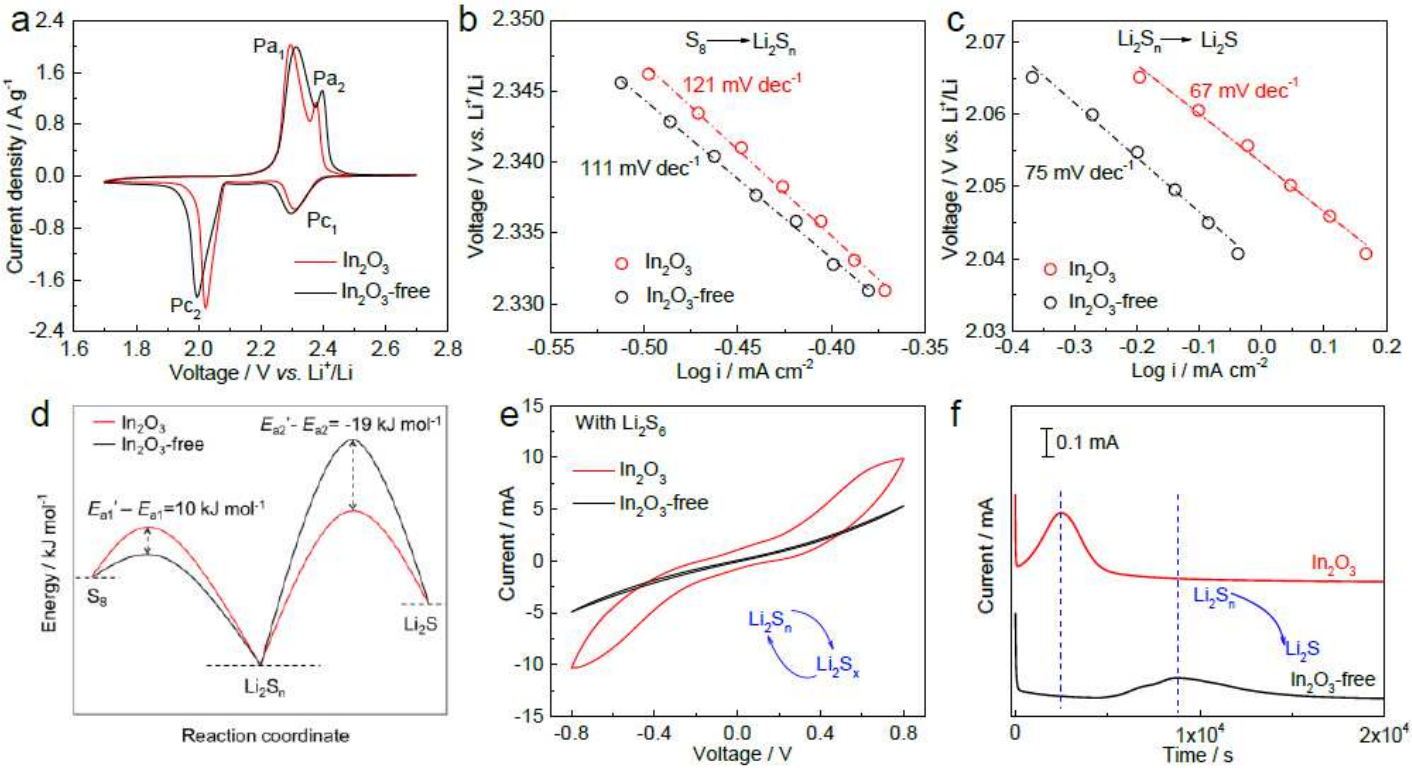

Figure 1

Electrochemical properties of In2O3-catalyzed cathode in comparison to the In2O3-free case. (a) the second cycle of CV profiles for the In2O3-catalyzed and In2O3-free Li-S cells at a low scan rate of 0.1 mV s−1 and (b, c) Tafel plots corresponding to the reductions of elemental sulfur to Li2Sn and Li2Sn to Li2S; (d) the relative activation energies of the two sulfur cathodes, where the In2O3-catalyzed cathode shows a higher energy barrier for the conversion from S8 to Li2Sn, but a lower energy barrier for the Li2Sn-to-Li2S conversion, in comparison to the In2O3-free case; (e) CV curves of symmetric dummy cells using In2O3-catalyzed and In2O3-free electrodes at a rapid scan rate of 20 mV s-1; (f) potentiostatic discharge curves of a Li2S8/tetraglyme solution at 2.05 V on the In2O3 catalyzed and In2O3-free electrodes.

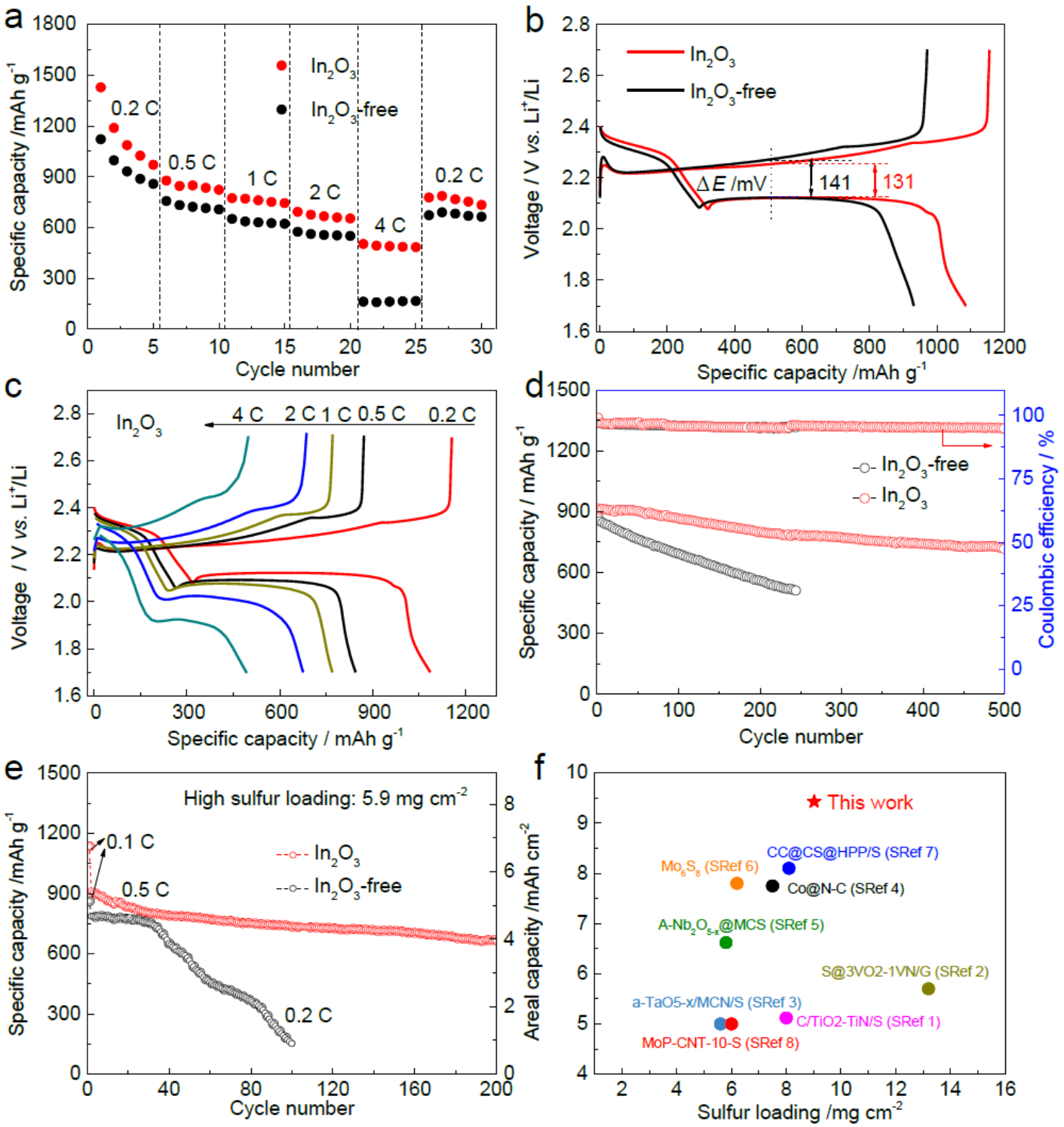

Figure 2

Electrochemical performance of In2O3-catalyzed Li-S battery in comparison to the In2O3-free battery. (a) rate performance (1C = 1675 mA g−1); (b) galvanostatic discharge-charge profiles at 0.2 C; (c) galvanostatic charge-discharge profiles of the In2O3-catalyzed battery at various current rates; (d) cycling stability at 0.5 C; (e) cycling performance with a high sulfur mass loading of 5.9 mg cm-2 at 0.5 C and 0.2 C; (f) a comparison with other sulfur cathodes with electrolyte/sulfur ratios ≤ 8 μL/mg (SRef: Supplementary References).

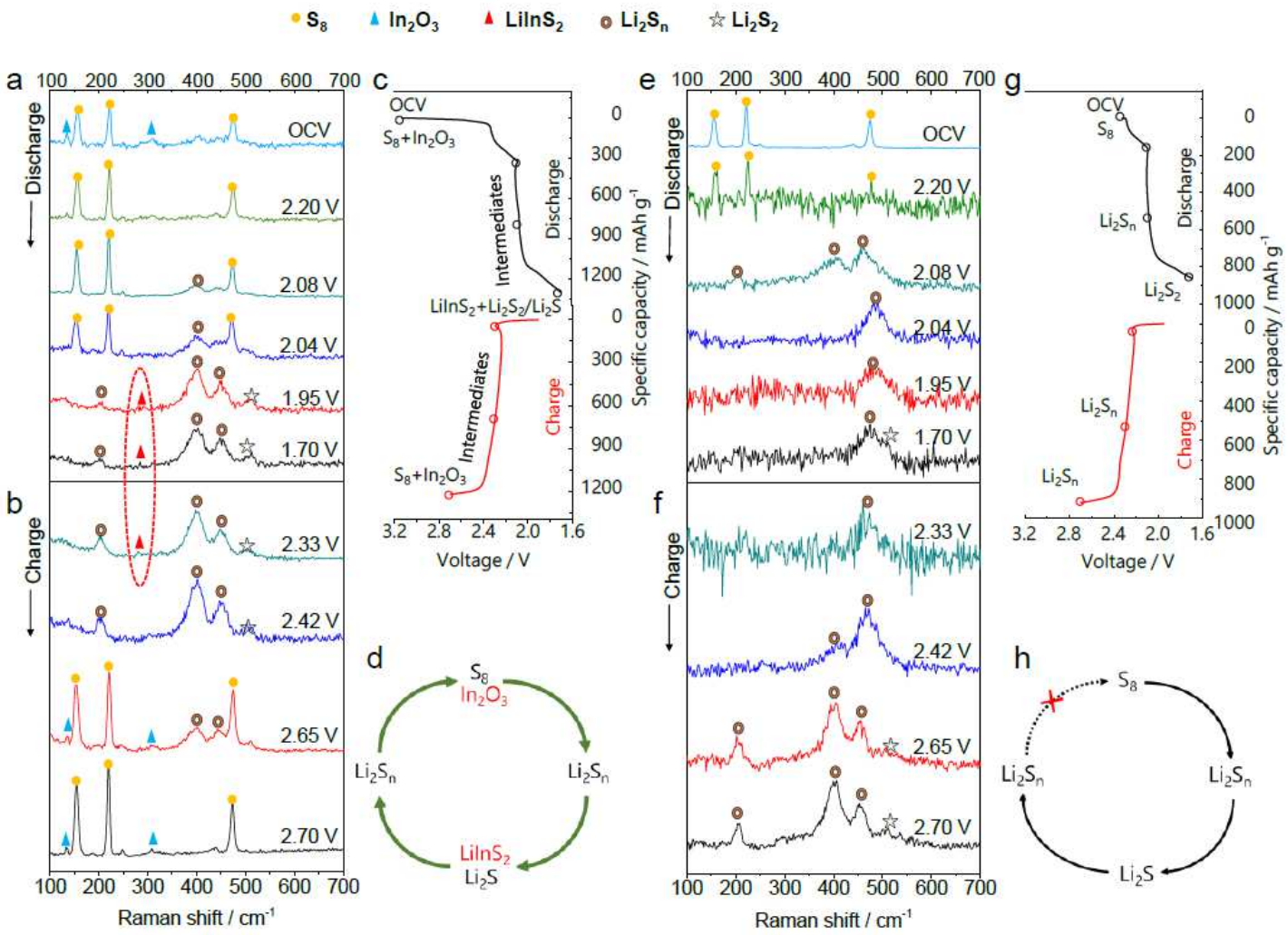

Figure 3

Reaction pathway demonstrated by in-situ Raman measurements. (a, b) Raman spectra of an In2O3-catalyzed battery and (c) the corresponding charge-discharge potentials of the detected substances; (d) a complete cycle of the sulfur redox with In2O3 catalyst; (e, f) Raman spectra of an In2O3-free battery and (g) the corresponding charge-discharge profile; (h) an incomplete cycle of the sulfur redox free of In2O3 catalyst. See more details in Supplementary Fig. 20.

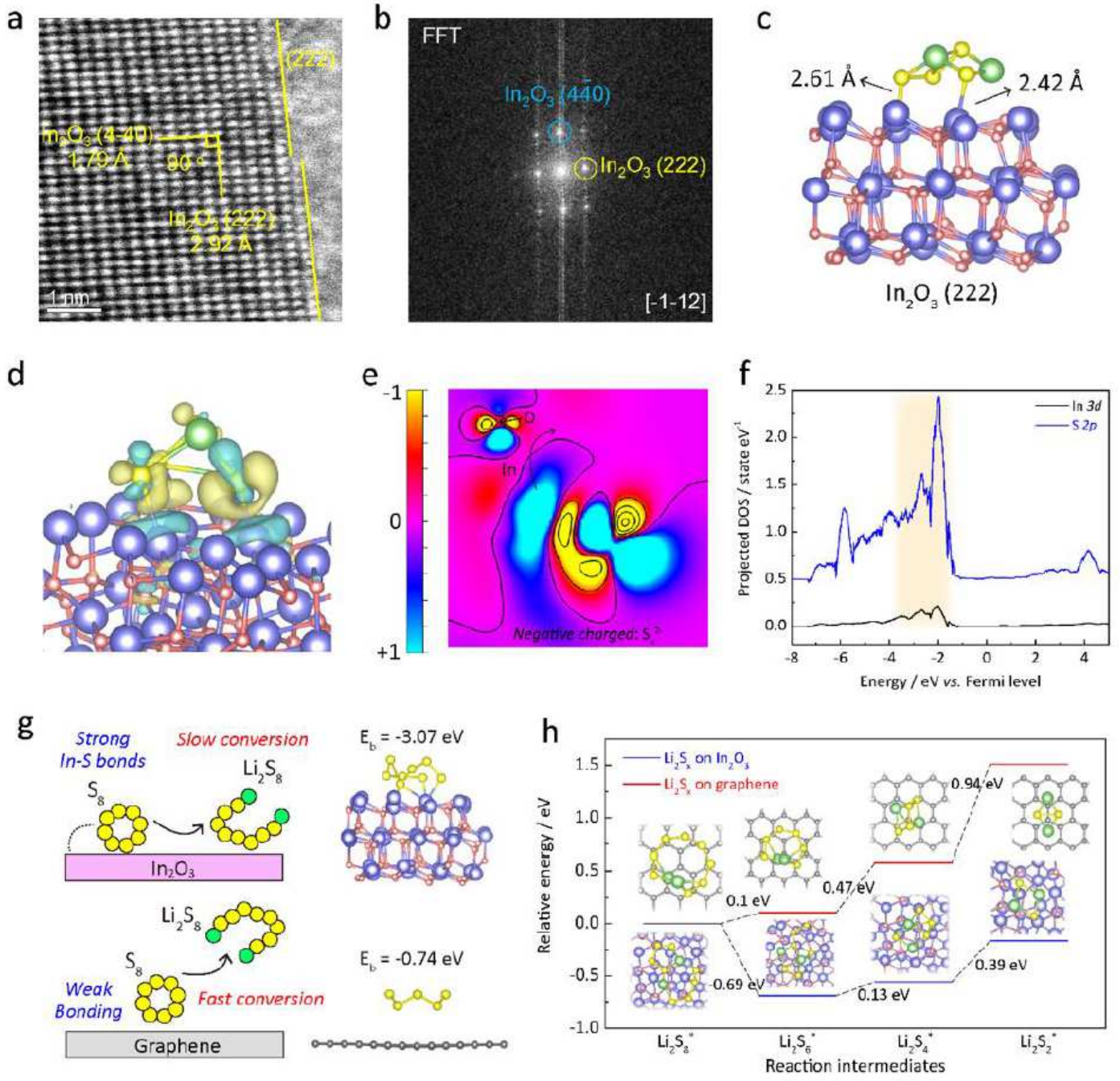

Figure 4

Computational simulation for the reaction pathway and LiInS2 intermediate. (a) ADF-STEM image of the G-In2O3 hybrids; (b) the superimposed FFTs of In2O3; (c) the optimized structure of Li2S4 on In2O3 surface; The In-S bond length are 2.42 and 2.61 Å, which are very close to the standard In-S bond length in LiInS2 (2.49 Å); (d) 3D charge difference of Li2S4 on In2O3; (e) 2D charge maps between In, O and S; (f) the projected DOS of In 3d and S 2p; (g) there is a much high binding energy of -3.07 eV between In2O3 and S8, compared to that of -0.74 eV of clean graphene substrate. Hence, S8 is hard to be desorbed from the In2O3 surface, and this slows down the conversion from S8 to Li2S8; (h) the reaction pathway from Li2S8*, Li2S6*, Li2S4* to Li2S2* intermediates on the In2O3 and graphene substrates.

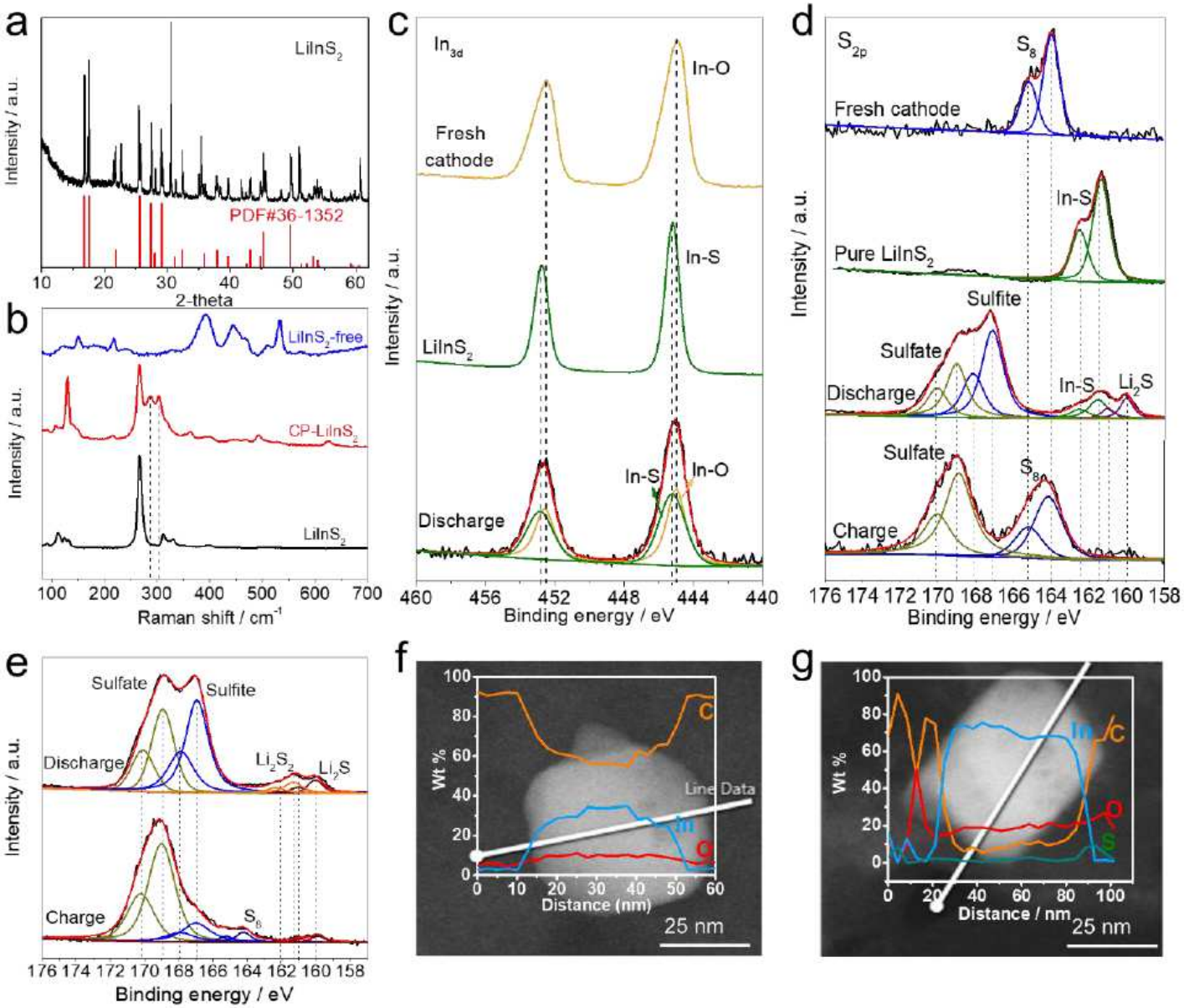

Figure 5

Conversion of polysulfide (Li2Sn) with LiInS2 as a catalysis intermediate. (a) XRD patterns of the prepared LiInS2; (b) Raman spectra (irradiated with 532 nm laser) of the synthesized LiInS2, LiInS2-free and LiInS2-based cathode (CP-LiInS2) discharged at 2.1 V; (c) XPS spectra for the 3d level of In: pristine In2O3, prepared LiInS2 and the In2O3 cathode in the fully discharged state; (d) S2p XPS spectra of fresh cathode, pure LiInS2 and the In2O3-catalyzed cathode in the fully discharged and charged state; (e) S2p XPS spectra of the In2O3-free cathode in the fully discharged and charged state; ADF-STEM images and corresponding line scan elemental mapping of (f) fresh In2O3 and (g) the In2O3-catalyzed cathode in the fully charged state.

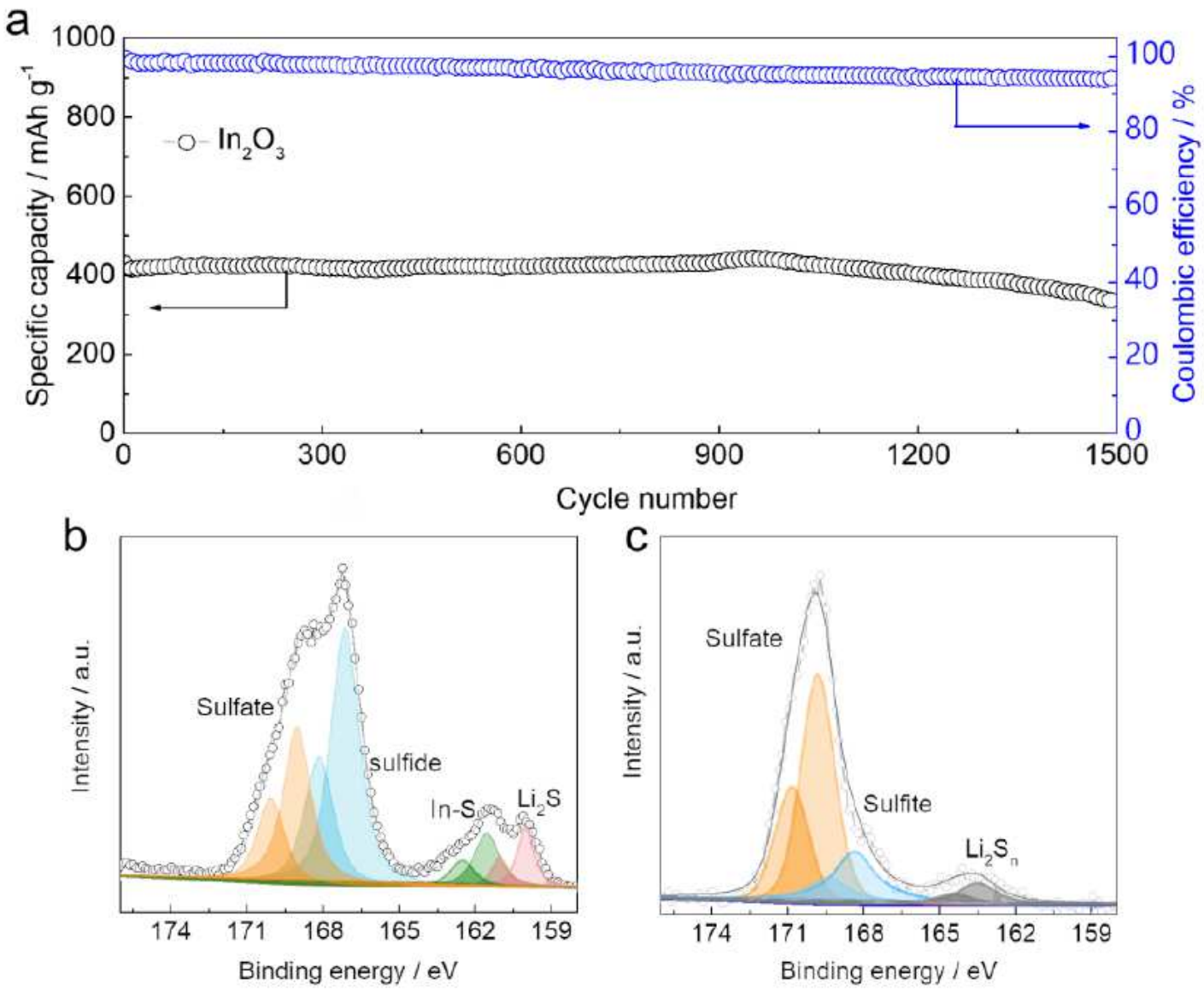

Figure 6

The deactivation of In2O3 catalyst. (a) cycling performance of In2O3-catalyzed battery at 4.0 C with a catalyst deactivation over 1000 cycles; S2p XPS spectra of In2O3-catalyzed cathode for the 1st (b) and 1000th cycle (b) in the fully discharged states.

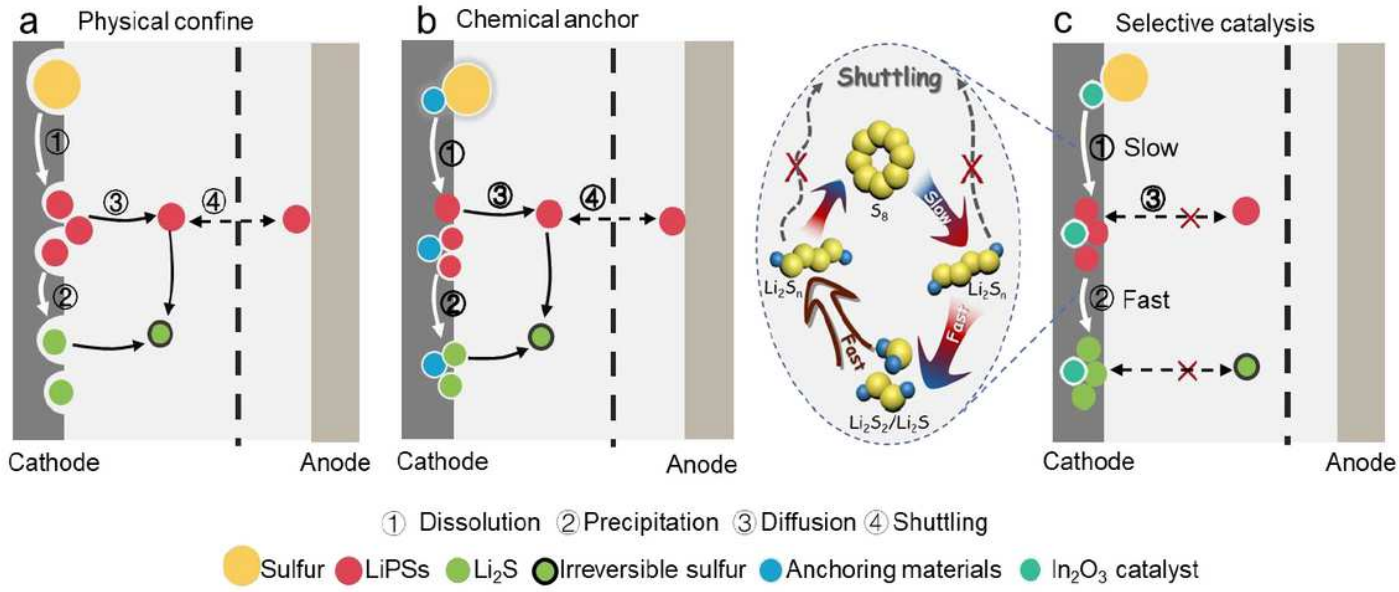

Figure 7

Scheme 1 Strategies to tackcle “shuttle effect” of soluble lithiium polysulfides (Li2Sn): physical confinement (a), chemical anchoring (b) and selective catalysis (c). Physical confinement and chemical anchoring are the most common ways to trap the soluble Li2Sn, working as follows: 1) the elemental sulfur gets electrons and forms Li2Sn on the conductive substrate; 2) the trapped Li2Sn are further reduced to Li2S on the conductive substrate; 3) other Li2Sn are released from the conductive substrate and dissolved in the electrolyte; 4) Some of the dissolved Li2Sn shuttle to the lithium metal side and then transfer back to the cathode side, resulting in the shuttle effect; the shuttled Li2Sn result in a continuous loss of active sulfur and the corrosion of Li anodes. Selective catalysis is proposed in this study as a fundamental remedy for reducing the accummulation of soluble Li2Sn and finally inhibiting the shuttle effect. For the discharging, the catalysis selectively slows down dissolution of elemental sulfur to Li2Sn while accelerates the deposition of Li2Sn into insoluble Li2S.

Supplementary Files

This is a list of supplementary files associated with this preprint. Click to download.

- ESINatureCatalysissubmit.docx